J. Fluid Mech. (1990), *vol.* 211, *pp.* 211–242
Printed in Great Britain

Vortex street impinging upon an elliptical leading edge

By ISMET GURSUL AND DONALD ROCKWELL

Department of Mechanical Engineering and Mechanics, 354 Packard Laboratory 19, Lehigh University, Bethlehem, PA 18015, USA

(Received 6 October 1988 and in revised form 23 June 1989)

The interaction of a Kármán vortex street with an elliptical edge is investigated experimentally. Basic types of interaction, as a function of scale and transverse displacement of the incident vortex street, are revealed using flow visualization. Unsteady pressure fields induced by these interactions are measured by a phase-averaging technique and correlated with the visualized flow patterns for basic classes of interactions.

For a generic vortex–edge interaction, measurements of the phase-averaged velocity field allow construction of streamlines and vorticity contours showing the details of the interaction, including distortion of the vortical structures near the edge. The pressure field is calculated from the measured velocity field and interpreted in relation to the vortical structures.

Simulation of flow visualization using the measured velocity field demonstrates possible misinterpretations related to the underlying vorticity field.

1. Introduction

Unsteady loading of a body in an unsteady shear flow arises from interaction of various types of unsteady vorticity fields with the surface of the body. These interactions are important in the areas of flow-induced vibration and noise generation. Among the types of vorticity field–body interactions, the case of a body in the wake of another body is of fundamental importance. Rotor blades passing through the wakes of stator blades in turbomachinery and tubes in the wakes of upstream tubes in a heat exchanger tube bank are typical examples of wake–body interactions.

The nature of the unsteady vorticity field–body interaction is predominantly affected by the scale and circulation of the incident disturbances. The scale of the incident vorticity field relative to the body dimensions is an important parameter which determines the type of interaction mechanism. Even if the turbulent character of the incident wake is ignored, the interaction of highly coherent vortices with the body remains an unclarified problem.

If the characteristic wavelength of the incident vorticity field is much larger than the scale of the body, the induced pressure on the body will be well correlated and its influence felt simultaneously over the entire body. Under these circumstances, the flow may be regarded as quasi-steady and it can be shown (Davenport 1977) that the fluctuating pressure will be proportional to $\rho U_\infty q'$, where q' denotes instantaneous fluctuating velocity. In this approximation, the acceleration-induced component of pressure is neglected; moreover nonlinear convective terms are neglected as well on the basis that q'/U_∞ is very small. This result gives a useful relation between pressure

and velocity fluctuation spectra, which is used in wind engineering applications (see Davenport 1977).

When the wavelength of the incident vorticity field is of the same order as the body scale, nonlinear and viscous effects may be important. Several classes of coherent vorticity field–leading edge interactions have been reviewed by Rockwell (1983). These quasi-two-dimensional vortex–edge interactions suggest the most crucial parameters: the circulation, which is related to the vortex scale; the degree of vorticity concentration; and the relative location of the incident vortex with respect to the leading edge. It is shown that unsteady pressure fields along the surface of the edge take the form of downstream travelling pressure waves having defined wavelengths (Kaykayoglu & Rockwell 1985). Of course, the ratio of the incident disturbance wavelength to the wavelength of the pressure wave on the body will be a function of the scale of the unsteady vorticity field as well as the mean vorticity field and its subsequent distortion by the leading edge. The amplitude and wavelength of this pressure wave will determine the loading in the leading-edge region and the associated noise radiation.

Experimental observations of vortex–leading edge interactions show a number of complexities. Typically, the vortical structures are subjected to rapid distortion near the body, and in some cases they may be severed (or distended) at the leading edge. Moreover, boundary-layer separation and secondary vortex formation may occur (Ziada & Rockwell 1982). In certain edge configurations, such as a finite-thickness leading edge (Sohn 1985), severing of the vortex has not been observed. All of these experiments were done with a mixing-layer configuration and the emphasis was on the pressure loading and flow visualization. For the analogous case of an unstable axisymmetric jet interacting with a cone aligned along the axis of the jet, similar types of interaction mechanisms have been observed. Vorticity contours show the features of flow separation induced by the incident axisymmetric vortices (Nelson 1986). Interaction of an axisymmetric vortex ring incident upon a flat plate oriented normal to the axis of the vortex was investigated by Didden & Ho (1984). Detailed measurements of the fluctuating vorticity field showed indications of flow separation and secondary vortex formation (see also Cerra & Smith 1983). To date, there has been no quantitative characterization of the classical interaction of a two-dimensional vorticity field with a leading edge, including phase-averaged vorticity distributions in conjunction with surface pressure measurements along the leading edge.

Although flow visualization suggests that changes in the unsteady vorticity field, such as distortion and severing of vortical structures, are possible, there is ambiguity of interpretation. In other words, how the distortion of a streakline or timeline pattern is related to the distortion of a vorticity field remains unclarified. If the flow marker (such as dye or smoke) is introduced well upstream, the visualized flow in downstream regions may have little to do with the real flow because the markers represent the integrated history of motion (e.g. Cimbala, Nagib & Roshko 1988). On the other hand, if the markers are introduced locally, some other aspects of misinterpretation, such as an appearance of amplifying streaklines in a neutral wave, are possible (Hama 1962; Gursul, Lusseyran & Rockwell 1989).

Simulation of vortex–edge interactions has been studied by several investigators. In order to gain physical insight, interaction of potential (point) vortices with plates (Rogler 1974), leading edges (Panaras 1985) and steps (Conlisk & Veley 1985) have been considered. These models involving point vortices cannot be expected to simulate all of the features of shear layers which have highly distributed vorticity.

For instance, rapid distortion and severing of the incident vorticity field near the tip region, and possible generation of secondary vortices, require separate modelling. However, these models can give physical explanations of certain aspects of the interaction. For example, the order of magnitude of the pressure fluctuations can be estimated in different flow regions (Rogler 1974). Panaras (1985) predicted pressure pulses as a result of the interaction of a discrete vortex with a ramp and an ellipse. In addition, he addressed the effect of the unsteady velocity potential on the pressure fluctuations.

Concerning the simulation of distributed vorticity field–leading edge interactions, a number of point vortices of small strength have been used to represent a finite-area vortex (Panaras 1987). This model proved to be successful for simulating the distortion of the vortical structures owing to the strain field induced by the presence of the body. Kaykayoglu (1987) has demonstrated that a similar model simulated selected features of the large-scale distortion as the body is approached.

However, all these discrete vortex simulations are inviscid and therefore assume that the boundary layer on the body is very thin and does not play a significant role in determining the flow structure. It is, however, known that all sources of vorticity for constant density flows are located on the boundaries (Morton 1984) and their strength is related to the tangential pressure gradients along the boundary. Since the leading edge is a region of large pressure gradients, generation of vorticity is concentrated around it. The strength of the vorticity sources at the leading edge will be time-dependent because of the unsteady pressure gradients. In fact, interaction of the incident vorticity field with the boundary-layer vorticity is an important aspect of this class of problems. Doligalski & Walker (1984) studied the interaction of a point vortex with an infinite wall for high Reynolds number. By using the unsteady boundary-layer equations, it was shown that boundary-layer separation occurs on the wall, followed by an eruption process. This means that the wall-layer vorticity is partly transferred into the outer flow.

The present investigation examines experimentally the interaction of a Kármán vortex street with an elliptical leading edge. The experimental techniques are summarized in §2. Different scales and relative locations of the incident vortex street are examined in §3, and the corresponding vortex–edge interactions are classified using flow visualization techniques. In §4, the phase-averaged unsteady pressure distributions on the surface of the edge are presented and correlated with the flow visualization. For the generic case of an incident vortex street aligned with the leading edge, the phase-averaged velocity field is studied in §5; instantaneous streamlines and vorticity contours are presented to show distortion of the incident vortices and an attempt is made to calculate the pressure distribution. In §6, the measured velocity field is used to simulate and reproduce the visualized interaction. Difficulties encountered in interpretation of flow visualization of the interaction are illustrated. Finally, the conclusions are summarized in §7.

2. Experimental system

Figure 1 shows an overview of the vortex street–edge arrangement. Details of the elliptical edge and the water channel are described by Sohn (1985). The elliptical leading edge has a ratio of major to minor axes of 5:1 and is attached to a long plate. During the experiments, the half-thickness of the body H and the free-stream velocity U_∞ were kept constant, while the offset distance ϵ and the wavelength λ_∞ of the undisturbed vortex street were varied. The vortex streets incident upon the

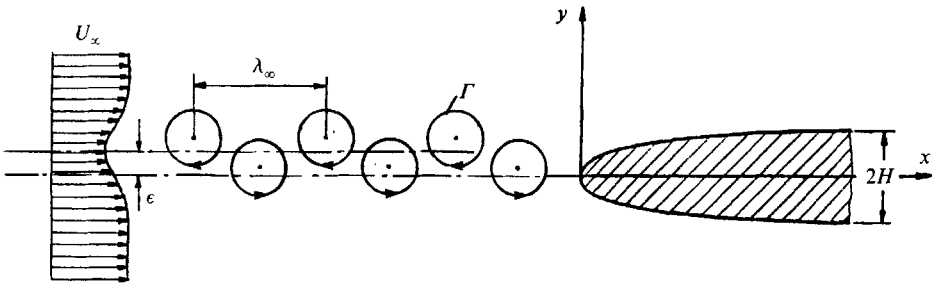

FIGURE 1. Vortex street–body arrangement.

elliptical edge were generated by using upstream plates with different thicknesses. The Reynolds number based on the plate thickness was in the range 309–619. The thickness of the body was $2H = 2.54$ cm, the free-stream velocity was $U_\infty = 9.65$ cm/s, and the distance between the upstream plate and the leading edge was $L/H = 12$.

The flow structure was visualized by dye streaklines only during the initial stage of the investigation. In the later stages (and in all the visualization pictures herein), the hydrogen-bubble technique was used. A vertical platinum wire of 0.025 mm diameter was placed at various locations upstream of the leading edge. As will be shown later, the location of the wire is important in interpreting details of the visualized flow. In all flow visualization shown herein, the wire is located at $x = -12$ cm ($x/H = -9.45$), unless otherwise noted. The duration time for hydrogen-bubble generation from the wire is adjustable by using a tuneable pulse generator. Finite duration time generates finite-thickness timelines, whereas continuous generation of the bubbles produces markers that correspond to streaklines. Lighting was provided by two 90 W stroboscopic lamps.

An Instar IV high-speed video system was used to record the visualized flow patterns. This system has a framing rate of 120 frames/s and a split-screen capability which allows simultaneous recording of the flow pattern and instantaneous traces of the pressure transducer outputs.

The unsteady pressure field was measured by using high-sensitivity Kulite pressure transducers (XCS-190-2D) with a Paralene coating. A total of 21 pressure taps were located along the leading-edge region of the semi-elliptical body, one at the tip and the others on the upper and lower surfaces. The diameter of each pressure tap was 0.79 mm. Channels connecting the taps to the transducers had a diameter of 1.59 mm and lengths ranging from 5.5 to 12.1 cm. A major concern was the amplitude and phase distortion of the pressure signal owing to the finite length of these channels. An extensive calibration method was devised to check this effect (Sohn 1985). An eccentric motor drive was used to displace a fixed volume of water sinusoidally in a cylindrical tank in order to produce pressure variations of desired frequency and amplitude. The leading edge was placed at the bottom of the tank. A reference pressure transducer was mounted rigidly next to the active tap of the edge. With this method, it was possible to record pressure signals from the tap under consideration and from the reference transducer. Cross-spectral analysis showed that there were maximum amplitude and phase distortions of 5% and 2° respectively.

Velocity measurements were performed with a single component laser-Doppler anemometer (LDA) driven by an Argon-ion, 2 W laser. It operates in the backscatter mode and has a beam expander to optimize the signal-to-noise ratio. The data rate

was high enough to allow use of the analog output of the counter of the LDA system. The diameter of the measuring volume was about 0.07 mm. Silicon carbide particles of 1.5 μm diameter were used as a seeding medium. Measurements could be acquired at a minimum distance from the surface of the leading edge of about 1 mm.

The velocity measurement grid consisted of 20 streamwise (x-axis, u-velocity) locations with variable spacing ranging from $\frac{1}{4}$ to $\frac{1}{40}$ of the wavelength in the undisturbed vortex street. In the cross-stream direction (y-axis, v-velocity), there were 30 measuring locations in increments of 1.27 mm. All measurements were carried out in the midplane of the flow; this plane also corresponded to the locations of the pressure taps on the surface of the edge. Unless otherwise noted, the instantaneous velocity is represented by a lower-case letter, the mean velocity by a capital letter, and the fluctuating component with a primed lower-case letter, e.g. $u = U + u'$. The same notation applies to vorticity.

For the pressure and velocity measurements, it was necessary to use a reference velocity signal; it was obtained from a hot film located at the upper edge of the shear layer of the incident vortex street. Cross-spectral analysis using a fast Fourier transform (FFT) method in a MINC minicomputer provided the amplitude and relative phase angles between the reference velocity signal and the desired velocity or pressure signal. For each cross-spectral analysis, 25 oscillation cycles were sampled and a total of six spectra were averaged to give the final values. This method of measurement gives phase-averaged quantities. The question arises as to how well a phase-averaged cycle of the pressure or velocity oscillation represents an individual cycle. This uncertainty can be estimated from the standard deviations for the ensemble-averaged amplitudes and phase angles. As addressed subsequently (see equation (3)), the fluctuation field is represented in terms of travelling waves. The uncertainties for the velocity field are estimated by performing a perturbation analysis (Gursul 1988). Using this approach, the uncertainties for the streamwise and cross-stream components are $\delta u = 0.03U_\infty$ and $\delta v = 0.05U_\infty$. Near the surface of the elliptical edge, the components normal and tangential to the surface were measured and the streamwise and cross-stream components were deduced from these measurements. The corresponding uncertainty for the amplitude of the cross-stream component is estimated as $\delta v_A = 0.08U_\infty$ in the worst case.

3. Flow visualization

The purpose of this part of the investigation was to explore and classify the basic mechanisms of interaction of the Kármán street with the elliptical leading edge. In these experiments, the free-stream velocity U_∞ was kept constant. The offset distance ϵ (figure 1), the wavelength λ_∞ in the undisturbed vortex street and the half-thickness of the body H determine the type of the interaction for a fixed aspect ratio ellipse. In general, it is possible to classify the flow–edge interactions based on the lengthscale of the flow represented by λ_∞/H. Two representative scales, designated as 'small-' and 'large-' scale vortex streets, were studied.

The interactions of the small-scale vortex street are shown in figure 2. The vortex street of two rows of alternating vortices impinges upon the body and one of two possible flow patterns exists: (*a*) the two rows are separated by the body ($\epsilon/2H = 0$ in figure 2); or (*b*) the two rows stay together after impingement ($\epsilon/2H = 0.39$ and 0.59 in figure 2). Further examination of values of $\epsilon/2H$ between 0 and 0.39 showed that there was no case for which each vortex in a given row is split at the leading edge. In other words, the wavelength between the vortices is so small that they are

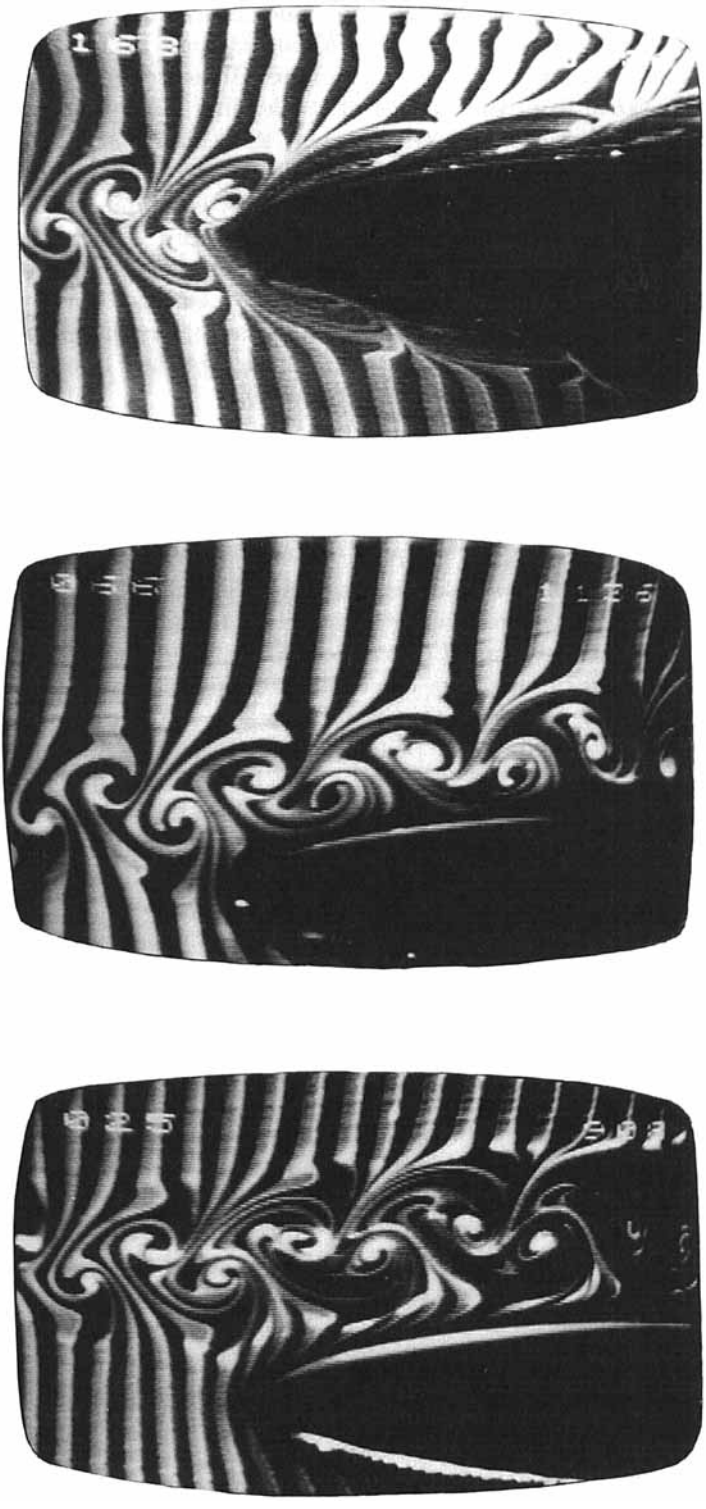

FIGURE 2. Interactions for small-scale vortex street $\lambda_\infty/2H = 0.81$.

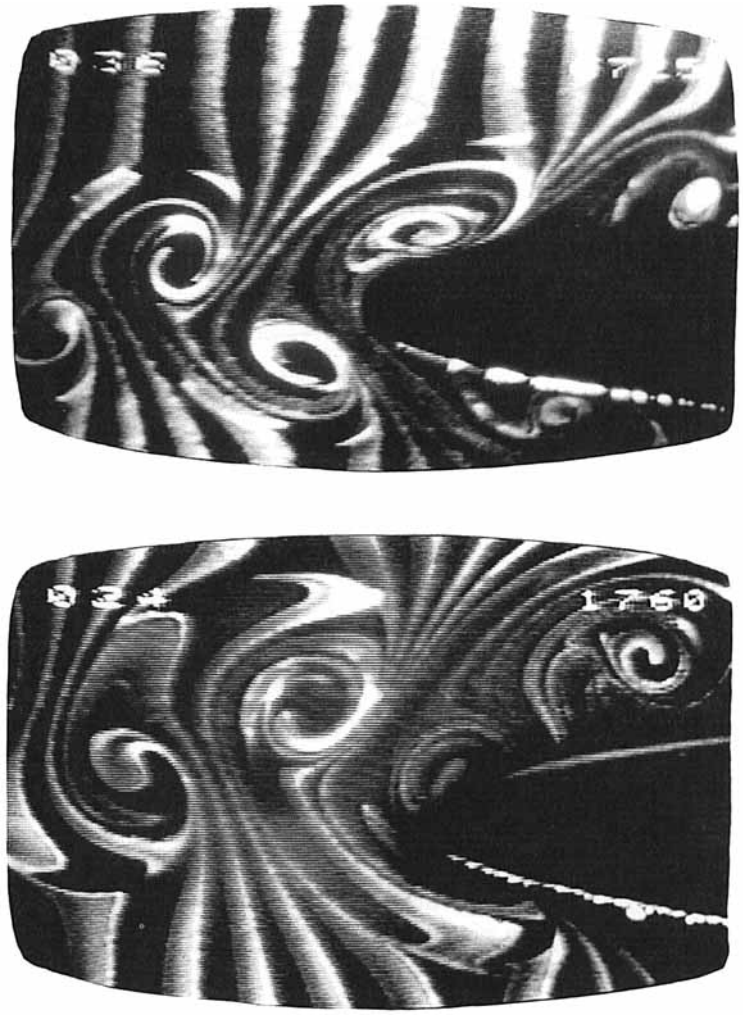

FIGURE 3. Interactions for large-scale vortex street $\lambda_\infty/2H = 1.62$.

convected along the body without splitting, even though they may be distorted substantially. Of course, for small values of $\epsilon/2H$, the distortion is greatest.

Figure 3 shows interactions of the large-scale vortex street for which the dimensionless wavelength is twice as large as the previous case. At $\epsilon/2H = 0$, the vortex street is divided in a similar fashion as for the case of figure 2. However, there is substantially less distortion of the individual vortices. In addition to the types of interaction described in figure 2, figure 3 (see also time sequence in figure 6*b*) reveals that an additional flow pattern is possible: each vortex in a given row is split into two while the vortices in the other row continue to move along the surface of the body.

In summary, there exist three basic vortex–edge interaction mechanisms as sketched in figure 4: (*a*) the vortex street preserves itself (case A); (*b*) the vortex street becomes two separate single rows of vortices (case B); or (*c*) one row of vortices is split and loses its identity as a row of vortices (case C). The first two of these possibilities are observed for both the small-scale and large-scale vortex streets, whereas the last one is inherent only to the large-scale street and is the most

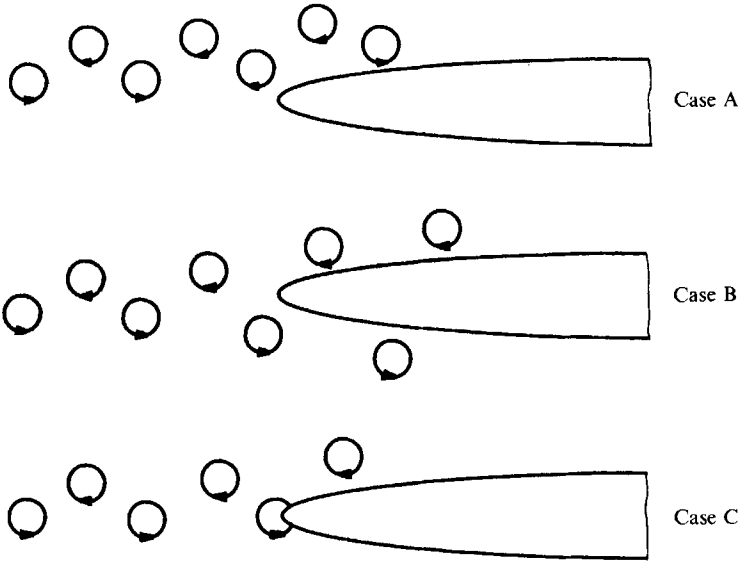

	$\epsilon/2H = 0$	$\epsilon/2H = 0.16$	$\epsilon/2H = 0.39$	$\epsilon/2H = 0.59$
$\lambda_x/2H = 0.81$	B	A	A	A
$\lambda_x/2H = 1.62$	B	C	A	A

FIGURE 4. Summary of flow visualization and different interactions.

complicated interaction. Of course, these interaction mechanisms determine the unsteady loading on the body. In the next section, the unsteady pressure field on the body will be related to the flow visualization.

4. Phase-averaged unsteady pressure field

Pressure measurements were carried out for the cases shown in figures 2 and 3. In general, the digitized time records of the measured pressure and velocity signals showed an essentially periodic character. Spectral analysis of the signals showed one dominant frequency, namely the Kármán street frequency, while the amplitude of the second harmonic was not more than 20% of this fundamental frequency component denoted as f. Therefore, the pressure fluctuation on the body can be approximated by

$$p'(x,t) = p_A(x)\cos(2\pi f t - \Phi_p(x)), \tag{1}$$

where p_A and Φ_p are determined from spectral analysis; and $\Phi_p(0)$ is determined from flow visualization performed simultaneously with the pressure measurements. From this information, it is possible to reconstruct the instantaneous pressure field and to relate it to the visualized flow pattern.

FIGURE 5. (*a*) Variation of pressure fluctuation amplitude for small- and large-scale vortex streets $\lambda_\infty/2H = 0.81$ and $\lambda_\infty/2H = 1.62$. (*b*) Variation of normalized pressure fluctuation amplitude for small-scale vortex street $\lambda_\infty/2H = 0.81$. (*c*) Variation of normalized pressure fluctuation amplitude for large-scale vortex street $\lambda_\infty/2H = 1.62$.

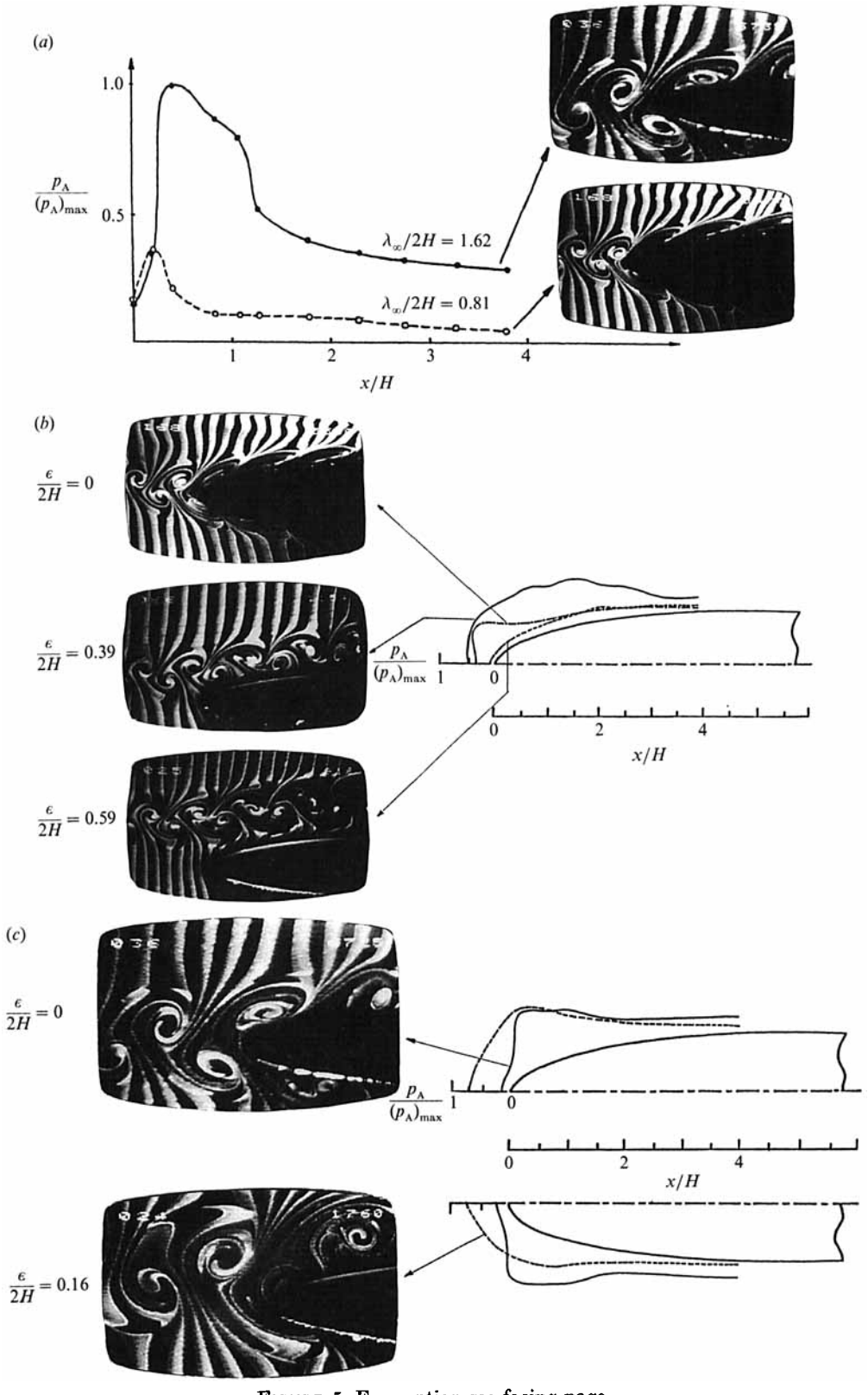

FIGURE 5. For caption see facing page.

	$\epsilon/2H = 0$	$\epsilon/2H = 0.16$	$\epsilon/2H = 0.39$	$\epsilon/2H = 0.59$
$\lambda_\infty/2H = 0.81$	0.08	—	0.10	0.03
$\lambda_\infty/2H = 1.62$	0.22	0.24	—	—

TABLE 1. Values of $(p_A)_{max}/\frac{1}{2}\rho U_\infty^2$ as functions of $\lambda_\infty/2H$ and $\epsilon/2H$

The order of magnitude of the pressure fluctuation amplitude varies strongly with the transverse location $\epsilon/2H$ of the incident vortex street as well as its lengthscale $\lambda_\infty/2H$. In all cases, U_∞ was kept the same in order to allow a direct comparison of the pressure amplitudes. For example, the distributions of the amplitude p_A for the small- and large-scale vortex streets in the case of $\epsilon = 0$ are compared in figure 5 (*a*) (in this figure $(p_A)_{max}/\rho U_\infty^2 = 0.11$). The similarity between these two distributions suggests a weak dependence on a characteristic Reynolds number $U_\infty \lambda_\infty/\nu$ in the range 2006–4012, and therefore implies a predominantly inviscid interaction.

The distributions of the normalized pressure fluctuation amplitude for different locations ($\epsilon/2H$) of the incident vortex street, but for the same scale $\lambda_\infty/2H = 0.81$, are summarized in figure 5(*b*). In this figure and all following figures, the magnitude of the pressure is proportional to the perpendicular distance from the surface of the body to the curve. Similarly, relative amplitudes for the large-scale ($\lambda_\infty/2H = 1.62$) vortex street are shown in figure 5(*c*). In the following section, the instantaneous pressure fields for each case will be reviewed individually. The pressure is normalized by its maximum value for each respective case under consideration. The values of maximum pressure fluctuation amplitudes for these cases are summarized in table 1.

4.1. *Interaction of small-scale vortex street*

In figure 6(*a–c*), the unsteady pressure fields and corresponding visualized flow patterns are shown for $\epsilon/2H = 0$, 0.39 and 0.59. For each case, three successive times with a time interval $\frac{1}{6}T$ are considered, where T is the period. The grid-hatched regions show the amplitude $p_A(x)$ and the cross-hatched regions indicate the instantaneous pressure $p'(x, t)$. Again, the magnitude of the pressure is proportional to the perpendicular distance from the surface to the curve.

In the case of zero offset ($\epsilon/2H = 0$), the amplitude distributions on the upper and lower surfaces are symmetrical within 5% accuracy and the phase difference is $\pi \pm 0.1$ radians. For this reason, only the upper part of the distribution is shown. In the tip region, the approaching vortex with a clockwise circulation causes a positive peak in the pressure fluctuation. For the most part, downstream of the tip of the leading edge, the vortex-induced pressure is similar to that of a point vortex past an infinite flat plate (Gursul 1988). Along this part of the edge the regions of negative pressure approximately correspond to the locations of the vortices.

For the cases of non-zero offset ($\epsilon/2H \neq 0$, see figures 6*b* and 6*c*), there is no sharp peak in the time-averaged pressure amplitude envelope (grid-hatched region). Although the absolute pressure amplitude differs substantially with the offset distance ϵ (see figure 5*b*), the interactions at $\epsilon/2H = 0.39$ and 0.59 are very similar. The gradual variation of pressure amplitude attains its maximum approximately at the location where the trajectory of the vortex street is closest to the body. This distribution of the pressure amplitude is very similar to that predicted by the discrete vortex simulation of Kaykayoglu (1987). The vortices of the lower row of the

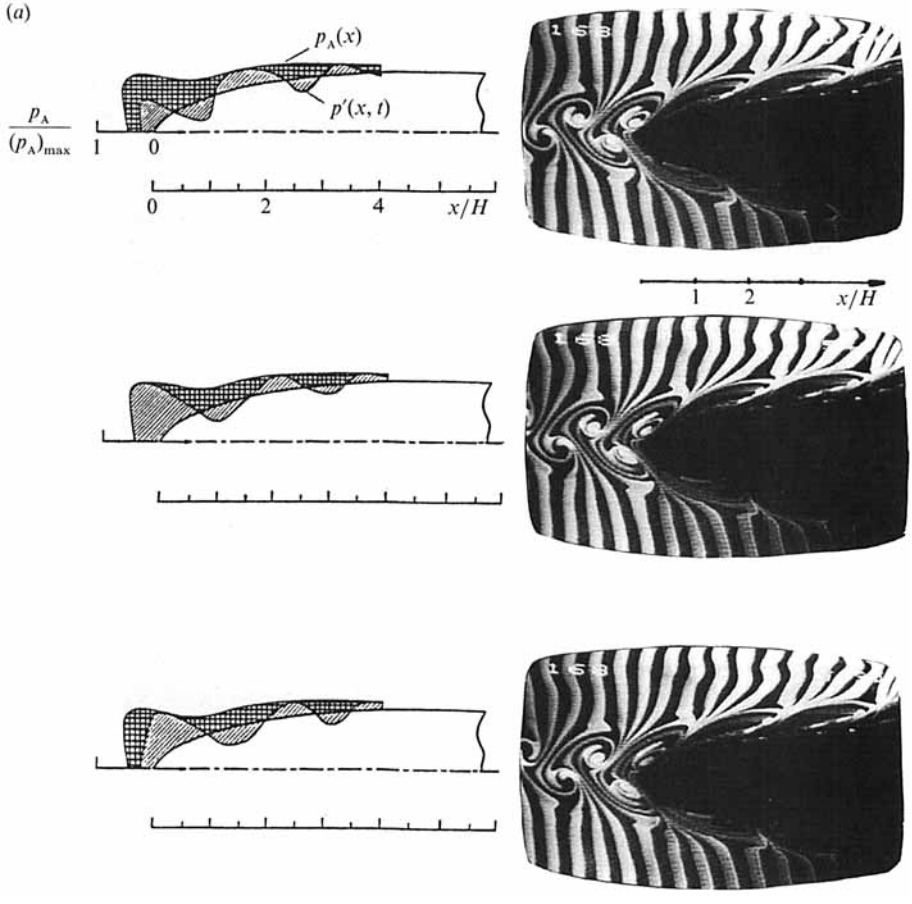

FIGURE 6. For caption see page 223.

Kármán street (with counterclockwise circulation) cause a negative peak in the unsteady pressure. For the case of zero offset ($\epsilon/2H = 0$), the vortices of the upper row (with clockwise circulation) give the same result. Therefore, the sense of the rotation has no effect on the phase of the induced pressure signal, which can be verified by considering a point vortex past an infinite flat plate (Gursul 1988).

4.2. *Interaction of large-scale vortex street*

In figures 7(*a*) and 7(*b*), the unsteady pressure field and the visualized flow patterns are shown for $\epsilon/2H = 0$ and 0.16 at three successive times. The time interval between the plots is one-sixth of the period T. In the case of $\epsilon = 0$ (figure 7*a*), substantial distortion of vortices in both the upper and lower rows is observed. The nature of the pressure field induced by each vortex on the lower side of the incident street is the same as on the upper side, except shifted in phase by π. All of the observations made for the corresponding small-scale interaction of figure 6 are valid here as well. Although the wavelength of the pressure fluctuation is twice as large as that of the small scale, the normalized amplitude distributions are very similar. This interaction of figure 7(*a*) is described in further detail subsequently.

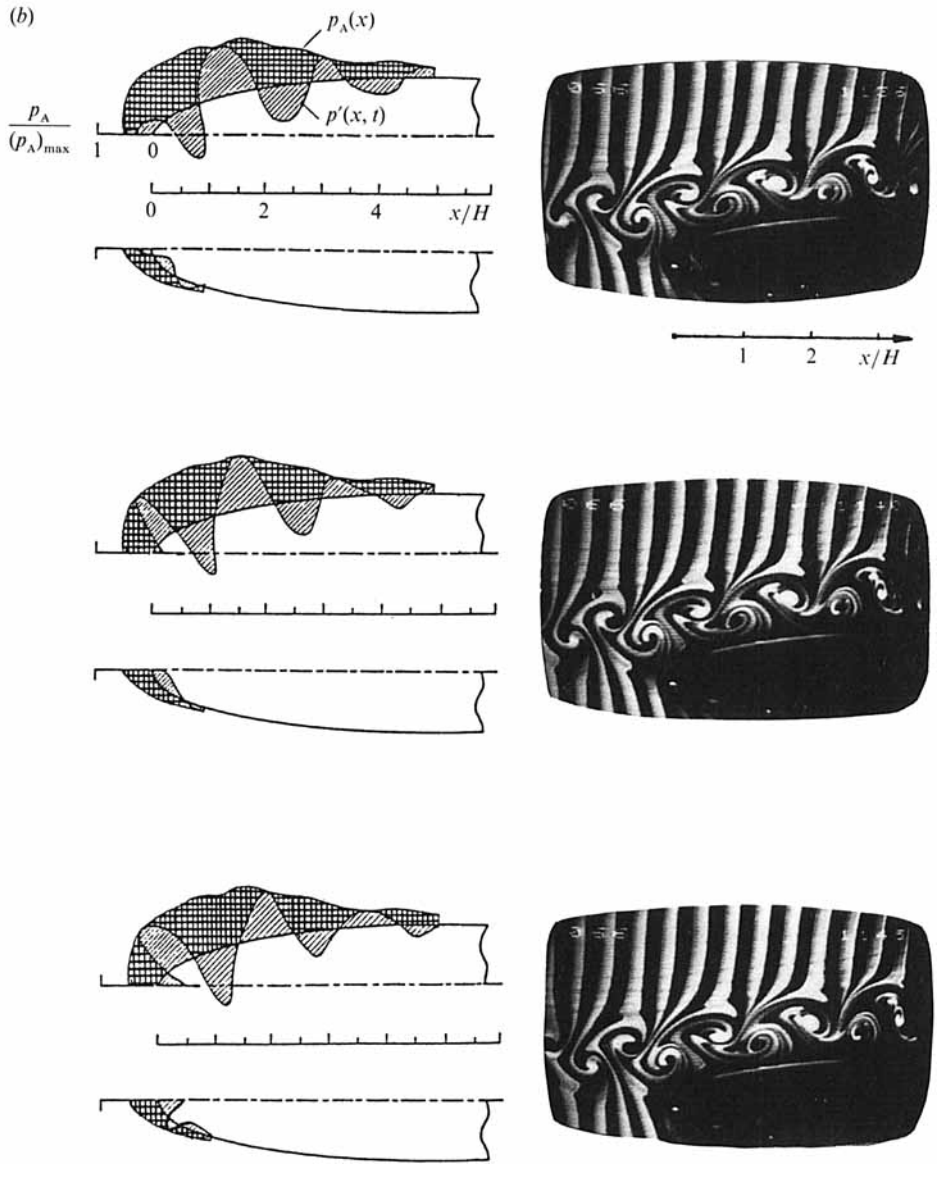

FIGURE 6. For caption see facing page.

The asymmetrical interaction ($\epsilon/2H = 0.16$) shown in figure 7(*b*) is more complex. While the vortices in the upper row are swept along the edge with minor distortion, those in the lower row are rapidly distorted, or distended. Concerning the tip region, figure 7(*b*) shows that the approaching vortex in the upper row with clockwise circulation induces positive pressure, and vice versa for the vortex in the lower row with counterclockwise circulation.

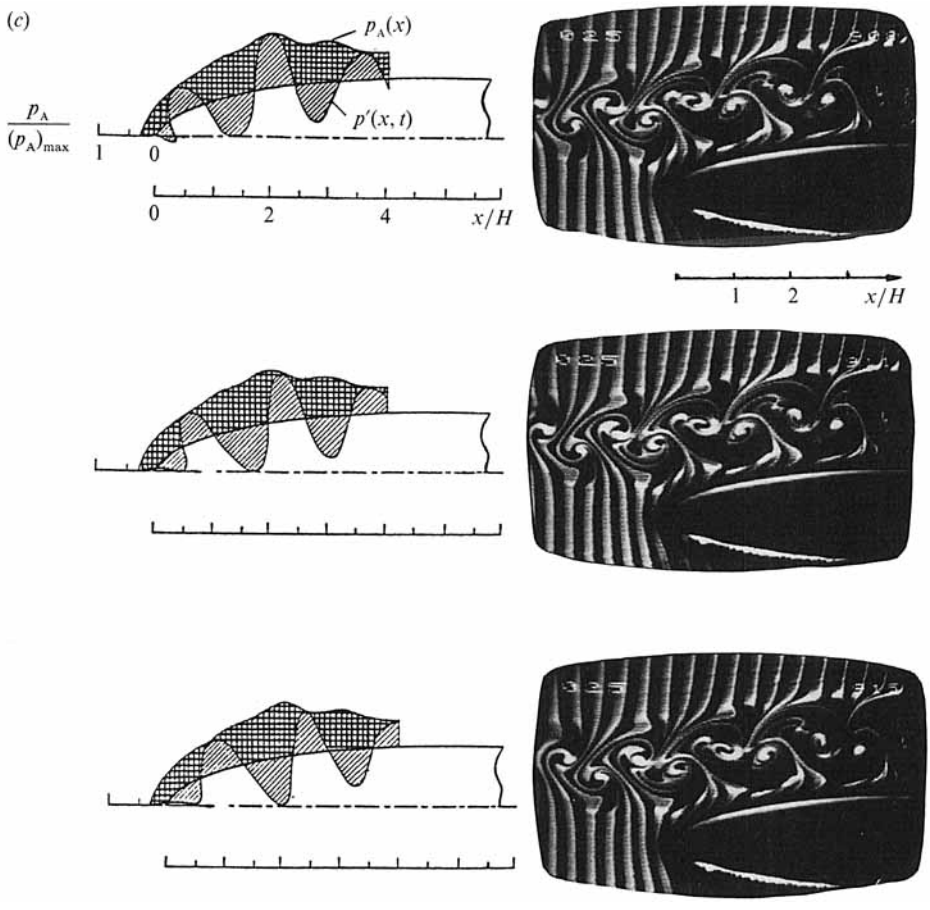

FIGURE 6 (*a*) Unsteady pressure field and corresponding visualized flow patterns for $\epsilon/2H = 0$ at three successive times separated by an interval $\Delta t/T = \frac{1}{6}$. $\lambda_\infty/2H = 0.81$. Grid-hatched regions and cross-hatched regions represent respectively amplitude and instantaneous value of pressure fluctuation. (*b*) Unsteady pressure field and corresponding visualized flow patterns for $\epsilon/2H = 0.39$ at three successive times separated by an interval $\Delta t/T = \frac{1}{6}$. $\lambda_\infty/2H = 0.81$. Grid-hatched regions and cross-hatched regions represent respectively amplitude and instantaneous value of pressure fluctuations. (*c*) Unsteady pressure field and corresponding visualized flow patterns for $\epsilon/2H = 0.59$ at three successive times separated by an interval $\Delta t/T = \frac{1}{6}$. $\lambda_\infty/2H = 0.81$. Grid-hatched regions and cross-hatched regions represent respectively amplitude and instantaneous value of pressure fluctuation.

5. Phase-averaged flow field

Detailed velocity measurements were carried out for the generic case of the larger scale Kármán street at zero offset, $\epsilon/2H = 0$ (see figure 1). The station at $x = -8.0$ cm is the upstream boundary of the measurement grid and lies within the region of the undisturbed flow. The mean velocity profile measured at this station is well fitted by a Gaussian profile.

$$\frac{U_\infty - U}{U_\infty - U_{CL}} = \exp(-aY^2), \tag{2}$$

where $Y = y/b$ and b is the half-width of the wake. Velocity U_{CL} is the value of U on the centreline. The constant a is taken as 0.693 in order to make $(U_\infty - U)/(U_\infty - U_{CL}) = 0.5$ at $Y = \pm 1$. In this experiment, the centreline velocity was equal to $0.81U_\infty$ and

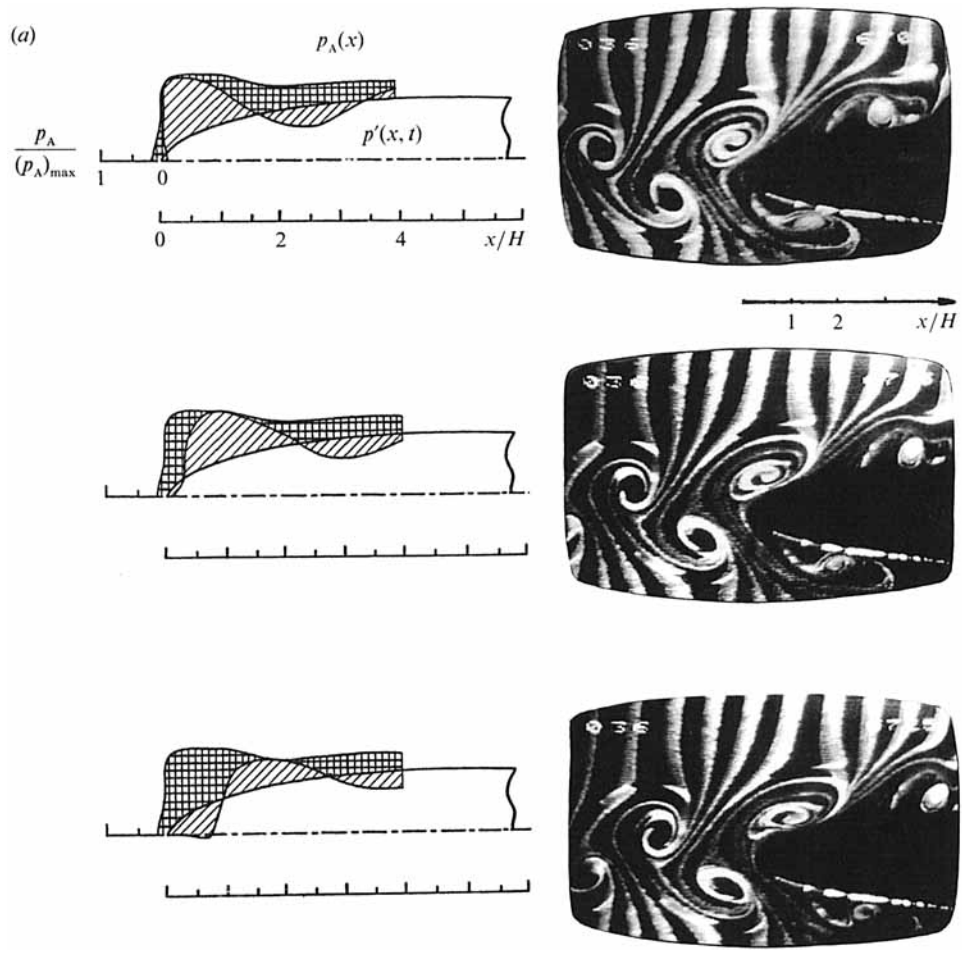

FIGURE 7. For caption see facing page.

$b = 6.35$ mm. From the measured velocity distribution, the calculated displacement thickness δ^* and momentum thickness θ were 2.83 mm and 2.49 mm, respectively. The Reynolds number based on the free-stream speed U_∞ and the momentum thickness θ was $U_\infty \theta/\nu = 243$. In order to make a comparison with the well-known wake regimes of a circular cylinder, an equivalent Reynolds number was obtained by equating the drag of the cylinder and the plate used in the experiments. Since the momentum thickness for the plate is known from the measurements, this provided a Reynolds number based on the diameter of about 300.

Using a hot-film signal as a reference, the amplitudes and relative phase angles could be obtained by cross-spectral analysis. The second harmonic component did not exceed $0.02U_\infty$ throughout the flow field and its amplitude derivative in the cross-stream direction was at least one order of magnitude smaller than that of the fundamental component. Therefore, considering only the fundamental component, the fluctuating velocity field can be approximated in the following form:

$$\left.\begin{aligned} u' &= u_A(x,y)\cos(2\pi ft - \Phi_u(x,y)), \\ v' &= v_A(x,y)\cos(2\pi ft - \Phi_v(x,y)), \end{aligned}\right\} \tag{3}$$

where Φ_u was taken as zero at $x = -8$ cm, $y = 0$ (see figure 1) and $f = 2$ Hz. It was

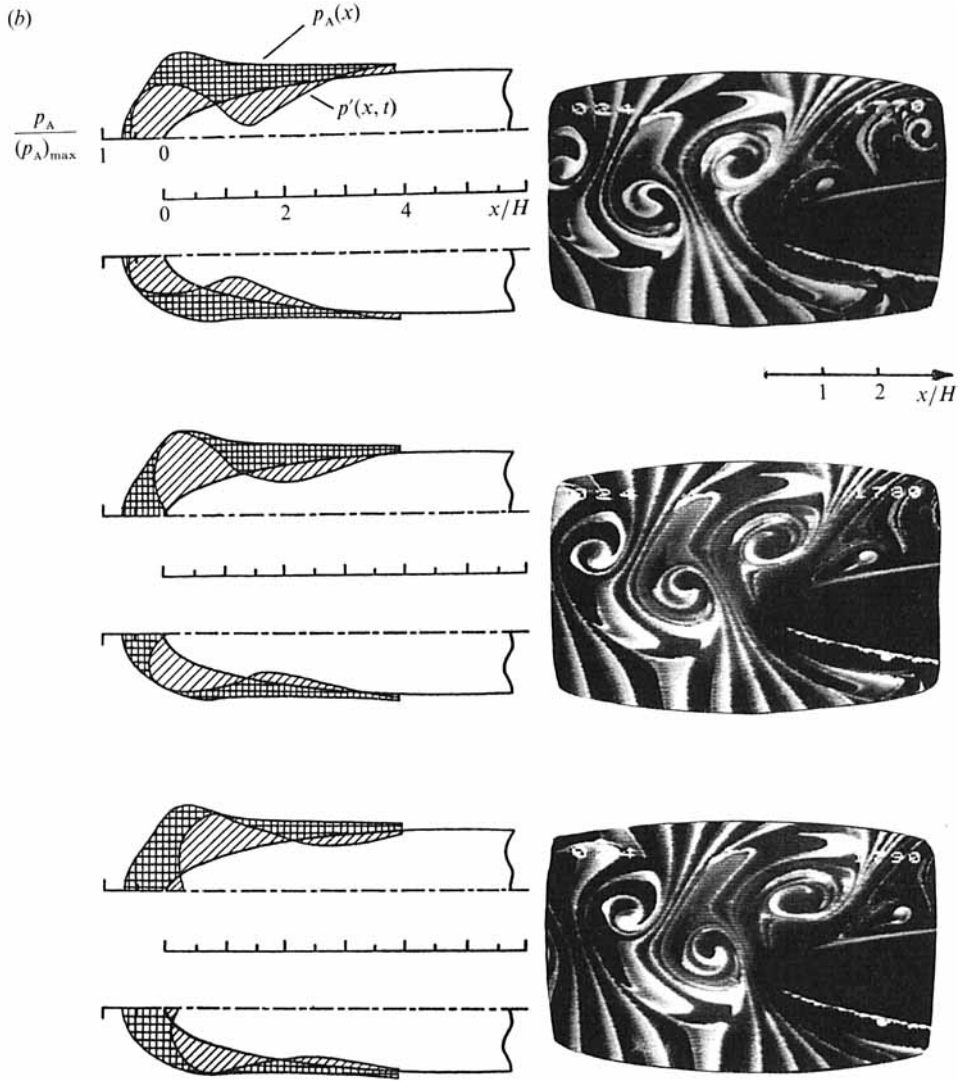

FIGURE 7. (*a*) Unsteady pressure field and corresponding visualized flow patterns for $\epsilon/2H = 0$ at three successive times separated by an interval $\Delta t/T = \frac{1}{6}$. $\lambda_\infty/2H = 1.62$. Grid-hatched regions and cross-hatched regions represent respectively amplitude and instantaneous value of pressure fluctuation. (*b*) Unsteady pressure field and corresponding visualized flow patterns for $\epsilon/2H = 0.16$ at three successive times separated by an interval $\Delta t/T = \frac{1}{6}$. $\lambda_\infty/2H = 1.62$. Grid-hatched regions and cross-hatched regions represent respectively amplitude and instantaneous value of pressure fluctuation.

observed experimentally that there is essentially a single frequency, the Kármán vortex shedding frequency, in the entire flow field.

Amplitude and phase angle distributions over the measurement domain are given in detail by Gursul (1988). The amplitude distributions well upstream are qualitatively similar to those of the neutral disturbance solution for oscillations in the 'sinuous mode' obtained from the Rayleigh equation for an inverted top-hat profile (Betchov & Criminale 1967). Measurements suggest that the neutral wave-like disturbance remains undistorted up to a distance of about half a wavelength from the

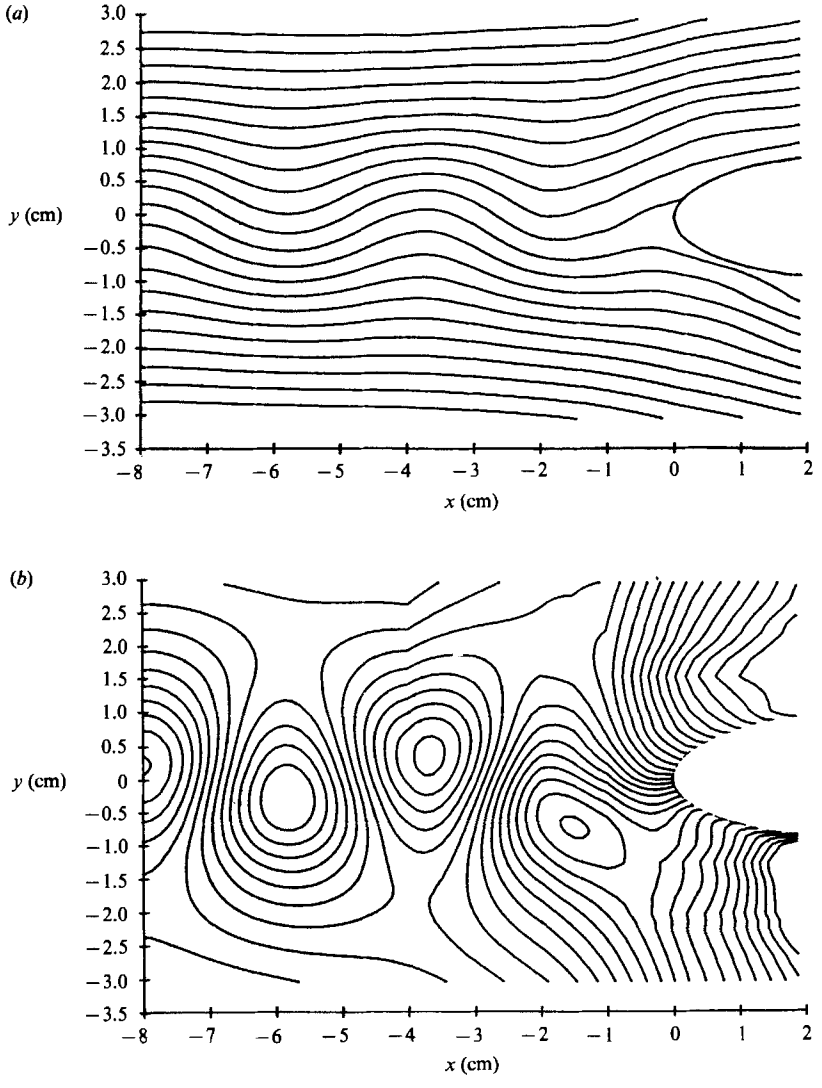

FIGURE 8. Instantaneous streamlines at $t = 0$ for: (*a*) a fixed laboratory frame; (*b*) a reference frame moving with the vortices, i.e. $U_{\text{ref}} = U_{\text{C}}$, where U_{C} is the average convection velocity of the vortices in the undisturbed vortex street.

leading edge of the body. Within the distortion region, large gradients of amplitude and phase are observed. The phase measurements provide information about the shape of the wavefront and the wavespeed of the disturbance as it travels downstream. When the phase speed U_{c} is calculated from

$$U_{\text{c}} = \frac{2\pi}{\partial \Phi_v / \partial x} f = \lambda f, \tag{4}$$

and averaged across the wake at $x = -8$ cm, the dimensionless phase speed is found to be $U_{\text{c}}/U_\infty = 0.90$.

The error due to measurement and discretization of the phase-averaged velocity

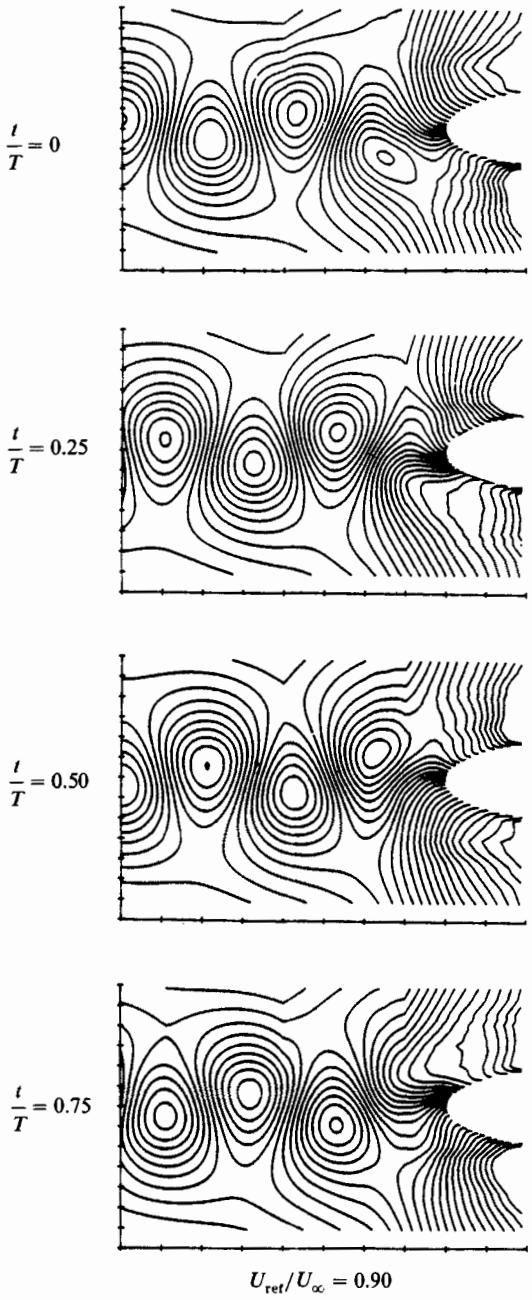

FIGURE 9. Instantaneous streamlines at successive times t during the period T of the incident vortex street for the reference frame moving with the vortices.

field is evaluated as follows. The residual ϵ_{ij} at any mesh point (i,j) is defined by (Imaichi & Ohmi 1983)

$$\epsilon_{ij} = \frac{(\partial u/\partial x + \partial v/\partial y)\,\delta x\,\delta y}{U_\infty\,\delta y}. \tag{5}$$

This quantity gives an estimate of the degree to which the continuity equation is satisfied, and therefore it is a measure of accuracy. The velocity gradients $\partial u/\partial x$ and

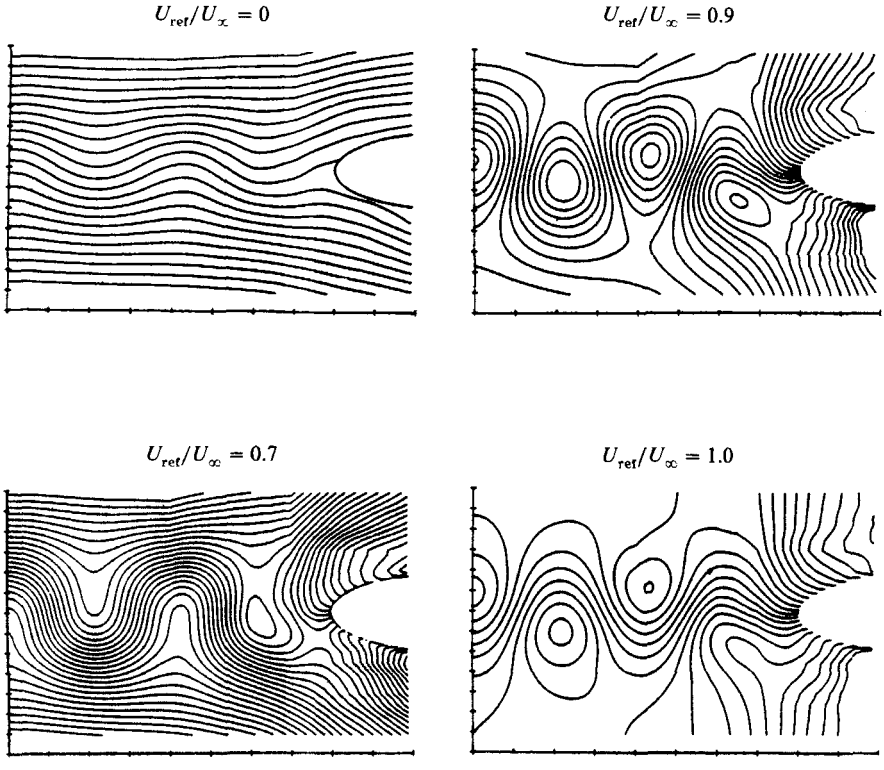

FIGURE 10. Effect of reference frame on the streamline patterns. In all cases, streamline pattern is at the same time $t = 0$.

$\partial v/\partial y$ are calculated by the central-differencing technique. The resultant distribution of $|\epsilon_{ij}|$ is given by Gursul (1988). In the undisturbed part of the vortex street, $|\epsilon_{ij}|$ is of the order of 2%. It is less than 5% everywhere except in the region very close to the body (within 1 mm) where it reaches a value of 10–20%. Therefore, it is concluded that the equation of continuity is well satisfied and the calculated derivatives are sufficiently accurate. Furthermore, the value of ϵ_{ij} is also a measure of the accuracy of the vorticity based on the velocity measurements, since the velocity gradients are calculated by the same finite-difference approximation.

5.1. *Streamline patterns*

Since the instantaneous total velocity field is known from equation (3), it is possible to calculate the instantaneous stream function ψ according to:

$$\psi(x, y, t) = \psi_0 + \int (u\,\mathrm{d}y - v\,\mathrm{d}x). \tag{6}$$

This line integral was evaluated numerically and ψ_0 was taken as zero at $x = -8$ cm, $y = -3$ cm. Figure 8(*a*) shows the streamline pattern at $t/T = 0$ (T is the period of the oscillation), which has a wavy shape. However, if the average convection speed of the undisturbed vortex street ($U_c/U_\infty = 0.90$) is removed, closed streamlines in a reference frame moving with the vortices are obtained (figure 8(*b*)). This phase-averaged flow field shows coherent structures having an appearance similar to the computed pattern of the von Kármán potential flow solution (Perry, Chong & Lim

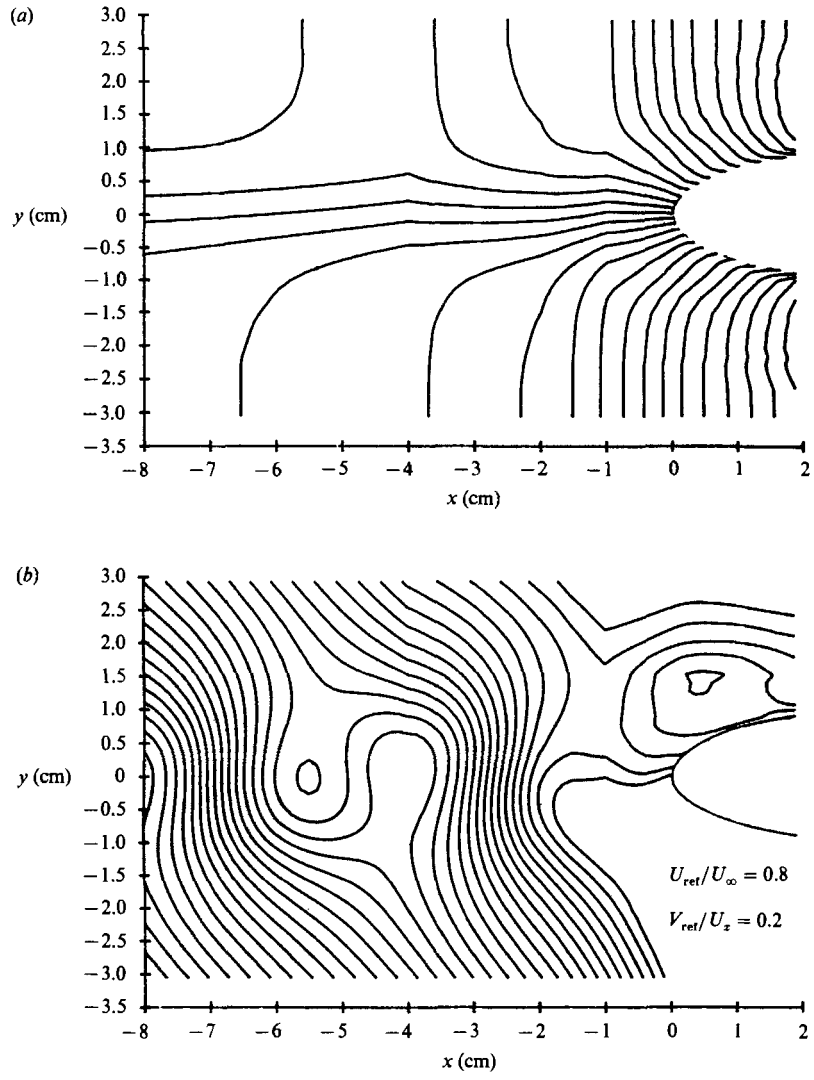

FIGURE 11. (*a*) Source-like behaviour of the leading-edge obtained by superposing $-U_\infty$ on the mean flow field, omitting the fluctuating contributions. (*b*) Streamlines (at $t = 0$) near the leading edge in a reference frame moving at an angle with the wake axis.

1982). It should be kept in mind that, in this frame, the body is not stationary; it has a speed of $-0.9U_\infty$. When the streamline patterns are studied at other times (figure 9) in this reference frame, the closed streamlines representing vortices seem to disappear near the body. Obviously, the choice of reference frame drastically changes the streamline pattern, and thereby one's impression of the vortex–body interaction.

Figure 10 shows, for a fixed time $t/T = 0$, the effect of reference frame on the streamline patterns. For all cases, closed streamlines disappear near the body. This can be explained by the presence of a 'source' effect; a leading edge in a uniform flow can be constructed by superposing a proper distribution of sources on the uniform flow. Therefore, when $-U_\infty$ is superposed on the entire flow field, only the source flow will be observed. (This is equivalent to observing the flow field in a reference frame moving with the velocity U_∞.) The streamline pattern in figure 11 (*a*) was obtained

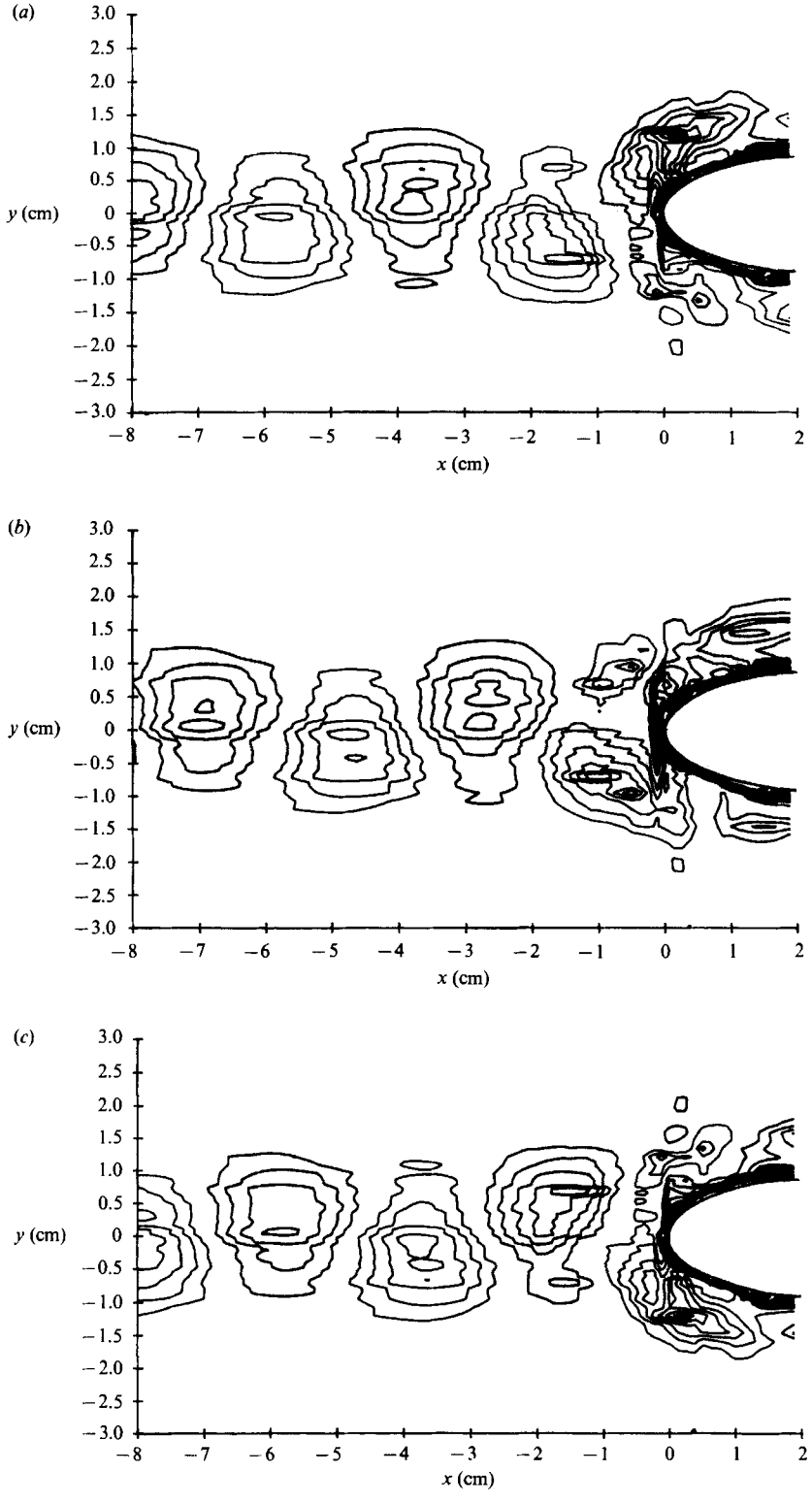

FIGURE 12. For caption see facing page.

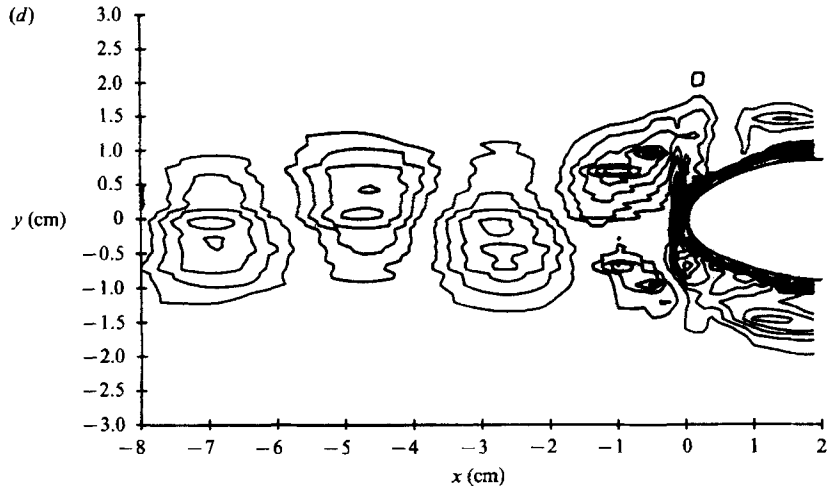

FIGURE 12. Contours of constant vorticity at; (*a*) $t/T = 0$, (*b*) 0.25, (*c*) 0.50 (*d*) 0.75. For all sets of vorticity contours, outermost contour has the same absolute value $\omega^* = 1.0$; increment between contour lines is $\delta\omega^* = 1.0$ ($\epsilon/H = 0$).

in this way; velocity $-U_\infty$ was superposed on the mean flow field and the fluctuating field was suppressed. In summary, the source-like behaviour of the leading edge dominates the unsteady field, resulting in the disappearance of the closed streamlines. However, from the calculated vorticity field (see figure 12), we know that local vorticity extrema are present at, and downstream of, the impingement region. Therefore, it should be possible to find a reference frame in which closed streamlines are present. Figure 11 (*b*) shows, for example, such a pattern in a reference frame moving at an angle with the wake axis.

Finally, the fact that streamlines in unsteady flows cannot give adequate information has been concluded by several investigators (e.g. Michalke 1964: Lugt 1979). Since streamlines are not invariant under the Galilean transformation, all possible reference frames should be considered at different times to locate the closed streamlines. Of course, greater insight is obtained by studying the vorticity field, which is invariant with the reference frame in which it is viewed.

5.2. *Vorticity field*

The component of the instantaneous vorticity normal to the (x, y)-plane was calculated from

$$\omega(x, y, t) = \frac{\partial v}{\partial x} - \frac{\partial u}{\partial y}, \tag{7}$$

using the central-differencing technique. After an estimate of the vorticity was obtained using the instantaneous velocity components, it was non-dimensionalized by U_∞/λ_∞:

$$\omega^* = \frac{\omega}{U_\infty/\lambda_\infty}, \tag{8}$$

and linear interpolation was used to plot the contours of dimensionless vorticity. An estimate of the uncertainty in the vorticity calculation owing to phase-averaging the flow field is presented by Gursul (1988). The standard deviation is around 1.0 (dimensionless) in the undisturbed vortex street and 3.0 near the body. This uncertainty in the undisturbed vortex street approximately corresponds to 20% of the maximum vorticity in the vortical structures approaching the edge.

Contours of constant dimensionless vorticity at four successive times during the period of interaction are shown in figure 12. For all sets of vorticity contours, the outermost contour has the same absolute value $\omega^* = 1.0$, which approximately corresponds to 20% of the maximum vorticity in the undisturbed vortex street; the increment between contour lines is $\delta\omega^* = 1.0$. Some dubious cases, for example, the existence of double peaks in a vortex (figure 12), might be caused by plotting algorithms as well as by random error.

Figure 12 shows that the vortical structures are 'frozen' in the undisturbed vortex street; in fact, this is a result of phase-averaging the flow field. However, it is known that disturbances undergo quasi-periodic oscillations in the nonlinear stage of free shear layers. For the wake flow in particular, this has been observed in experiments (Sato & Kuriki 1961) as well as in numerical simulations (Zabusky & Deem 1971), which showed that the low-frequency nonlinear oscillation is associated with the nutation of the principal axis of an elliptical vortex with respect to the mean flow. Note that the vortices tend to be elliptical in cross-section with a vertical major axis. (See the streamline patterns in figure 8.) Similar shapes of frozen structures have been obtained in a turbulent wake by directly using Taylor's hypothesis (Davies 1976). A nearly circular shape might arise if many vortices having random orientations are averaged.

An integral property of the vortex street which can be estimated from these results is the circulation of a typical vortex in the undisturbed vortex street. The circulation calculated as a line integral around a contour which encloses the vortex and passes through points of zero vorticity is $\Gamma/U_\infty \lambda_\infty = 0.51$. Another important parameter is the ratio of the maximum total vorticity to the maximum mean vorticity:

$$\gamma = \frac{\omega_{\max}}{\Omega_{\max}}. \tag{9}$$

It has a value of 8.0 and is consistent with the values reported in the literature (Hussain 1986).

When the vorticity contours are studied at successive times (figure 12), it is evident that the vortices are subjected to rapid distortion near the edge, deforming into elongated structures. The vortices become elliptical with their major axes parallel to the mean flow around the edge. This deformation, due to the strain field near the edge, takes place over a distance of about half a wavelength, which is the extent of the upstream distortion for this interaction. During encounter with the edge, the vortical structures are split; a portion of the negative vorticity (of the upper vortex) is swept along the lower surface of the body (see figure 12*a*). However, from inspection of the vorticity contours, it is apparent that the original vortex loses little circulation. The extremum of the vortical structure follows a trajectory resembling a streamline of the mean flow.

From detailed phase measurements (Gursul 1988) near the tip of the edge, the streamwise convection velocity U_c changes in the cross-stream direction from a small value ($U_c/U_\infty \approx 0.35$) at the centreline to a larger value ($U_c/U_\infty \approx 0.98$) at the edge of the shear flow. Because of this variation in the convection velocity, the portion of the vortex near the tip moves slower than its central portion. Eventually, this slowly moving portion of the vortex impinges upon the tip of the edge while the central portion is swept along the surface of the body (see figures 12*b* and 12*c*). This process gives rise to the elongation of the vortical structure.

It is of interest to compare the magnitudes of the vorticity in the incident vortex and the boundary layer. The boundary-layer thickness for the corresponding steady

flow (Schlichting 1979) for this elliptical leading edge is predicted to be around 1.5 mm. The order of magnitude of the mean vorticity within the boundary layer is U_∞/δ, which is approximately 30 times larger than the vorticity in the incident vortices. Therefore, the vorticity within the vortices convected by the mean flow is small compared to the large vorticity in the wall layer, which is confined to a very small region near the body. Note that there is no boundary-layer separation. Numerical simulations and experiments show that the vortex Reynolds number $Re = \Gamma/\nu$ must be sufficiently large in order to induce separation (Ersoy & Walker 1985; Peace & Riley 1983; Harvey & Perry 1971). In the present experiment, $Re = \Gamma/\nu$ was around 2200.

5.3. *Pressure field*

The instantaneous pressure field was calculated by substituting the measured velocity field (equation (3)) in the Navier–Stokes equations. The derivatives $\partial u/\partial t$ and $\partial v/\partial t$ can be evaluated from (3). The spatial derivatives were calculated by the central-differencing technique. From the Navier–Stokes equations, the pressure gradients $\partial p/\partial x$ and $\partial p/\partial y$ were computed at any desired time. In the undisturbed part of the vortex street, these gradients are of the same order. Near the body, the streamwise pressure gradient $\partial p/\partial x$ is usually larger than the cross-stream pressure gradient $\partial p/\partial y$. In order to find the pressure distribution, the pressure at the point ($x = -8$ cm, $y = -3$ cm) was assumed to be zero ($p_\infty = 0$) and the computed pressure gradients were numerically integrated:

$$p(x, y, t) = p_\infty + \int \left(\frac{\partial p}{\partial x} \mathrm{d}x + \frac{\partial p}{\partial y} \mathrm{d}y \right). \tag{10}$$

Depending upon the integration path, the difference between two integrated values of pressure was as large as $0.1\rho U_\infty^2$. Measurement error and discretization error lead to the error for the calculated pressure gradients at any mesh point. Moreover, the integration process gives rise to accumulated error. Similar difficulties in the calculation of pressure from the experimental velocity data have been reported in other studies (Imaichi & Ohmi 1983; Mathioulakis & Telionis 1987).

In order to avoid an integration process, another approach was taken. The Poisson equation for pressure, which can be derived from the Navier–Stokes equations, is:

$$\nabla^2 p = \frac{\partial^2 p}{\partial x^2} + \frac{\partial^2 p}{\partial y^2} = 2\rho \left(\frac{\partial u}{\partial x}\frac{\partial v}{\partial y} - \frac{\partial u}{\partial y}\frac{\partial v}{\partial x} \right). \tag{11}$$

The source term on the right-hand side can be calculated from the velocity field. The boundary conditions for the computational domain are as follows. At the bottom boundary ($y = -3$ cm), the pressure values are found by integration:

$$p(x, y = -3 \text{ cm}, t) = p_\infty + \int \frac{\partial p}{\partial x} \mathrm{d}x.$$

On all other boundaries, the normal derivatives are calculated from the momentum equations, i.e.

$$\partial p/\partial x (x = -8 \text{ cm}, y, t),$$
$$\partial p/\partial y (x, y = 3 \text{ cm}, t),$$
$$\partial p/\partial x (x = 2 \text{ cm}, y, t),$$
$$\partial p/\partial n,$$

on the body surface (the symbol n refers to the normal direction at the boundary).

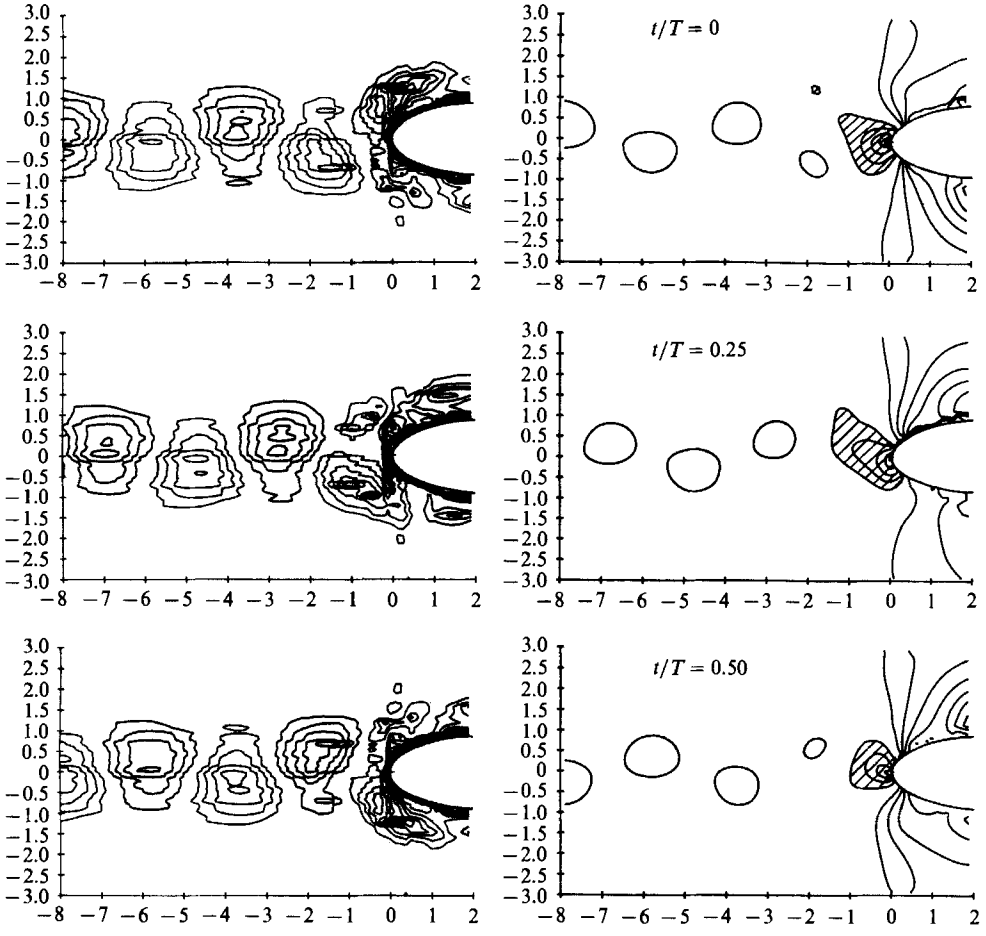

FIGURE 13. Contours of vorticity (left-hand column) and dimensionless pressure (right-hand column) at successive times $t/T = 0$, 0.25, and 0.50. Regions of positive pressure are shaded. The smallest absolute value of pressure contour levels is $p^* = 0.05$ and the increment between contour lines is $\delta p^* = 0.05$ ($\epsilon/2H = 0$).

Then, at any instant, the Poisson equation subject to these boundary conditions is solved by using an iterative method (successive over-relaxation).

In figure 13, the contours of vorticity in the left-hand column and the contours of dimensionless pressure $p^* = p/\rho U_\infty^2$ in the right-hand column are shown at three successive times $t/T = 0$, 0.25 and 0.50. The regions of positive pressure are shaded. The smallest absolute value of the pressure contour levels is $p^* = 0.05$ and the increment between contour lines is $\delta p^* = 0.05$. Because of the method used to calculate pressure, the contours of constant values of pressure are smooth in spite of the expected error at each node of the grid. In the regions where the source term of equation (14) is small, the value at each grid point is approximately the average of the values of the four neighbouring points. Therefore, the error is distributed more evenly.

Upstream of the interaction region, the negative pressure regions corresponding to the vortical structures are consistent with the vorticity contours shown in the left-hand column. However, these closed contours of negative pressure disappear near the body where strong pressure gradients exist. Deceleration of the mean flow near

the stagnation point of the body causes a large area of positive pressure. Along the surface of the body, this region is followed by a region of negative pressure. The absolute value of the negative pressure contour levels increases in the downstream direction. Considering only the unsteady pressure field, vortices cause a negative pressure fluctuation on the surface of the body (either upper or lower surface) as they approach the surface. This is evidenced by an increase in the number of negative pressure contours adjacent to the surface (see, for example the upper surface at $t/T = 0.25$). At this instant, there is a decrease in the number of negative pressure contours around the lower surface, which corresponds to a positive peak in the pressure fluctuations. Inspection of the plots at $t/T = 0$ and $t/T = 0.50$ reveals that the pressure distributions show antisymmetry for upper and lower surfaces, implying π phase shift between the pressure fluctuations on the surfaces.

The estimated uncertainty in the region away from the surface is around $0.05\rho U_\infty^2$. Since the error ϵ_{ij} increases near the body, no attempt was made to calculate the amplitude of the pressure fluctuations along the surface.

6. Flow visualization simulation

It was concluded from the vorticity contours that the vortices are subject to distortion near the body, deforming into elongated structures. This change in shape was due to the straining field of the edge. In fact, the flow visualization study (figure 7*a*) suggests similar distortion.

However, the streakline pattern for a potential (line) vortex impinging upon a corner (Conlisk & Veley 1985) shows similar elongation. Therefore, in laboratory flows, the interpretation of visualization of distributed velocity fields encountering leading edges has remained unclarified. In this section, an attempt will be made to examine some aspects of flow visualization and its interpretation.

Since the instantaneous total velocity field is known from measurements represented by (3), it is possible to track the particles of the defined flow, leading to the timelines and streaklines. Because the velocity was measured only at discrete points, bilinear interpolation was used to obtain the velocities at any arbitrary point. To integrate the equations of motion of the particles, i.e.

$$\frac{\mathrm{d}x}{\mathrm{d}t} = u(x, y, t), \quad \frac{\mathrm{d}y}{\mathrm{d}t} = v(x, y, t), \tag{12}$$

the Euler method was used with a timestep of one-hundredth of the period of the flow. To generate a timeline, a row of N particles are marked on the line $x = x_0$ at $t = t_0$. The timeline at $t = t^*$ is then obtained by connecting these particles. Generating and connecting rows of particles at a certain frequency creates a set of timelines moving in the downstream direction. On the other hand, generating a succession of particles from a given location until a time $t = t^*$, and connecting them, provides a streakline.

Figure 14 shows the vorticity contours and the streakline patterns at successive times $t/T = 1.5$, 1.75, 2.0 and 2.25, after the marker is injected at the left-hand boundary of the measurement grid. The simulated streaklines give the impression of an amplifying disturbance near the left-hand boundary. The apparent 'roll-up' of the streaklines is followed by their distortion and segregation during impingement upon the edge. From this visualization, it is difficult to predict the locations of the vorticity extrema; moreover, the apparent size of the streakline 'roll-ups' are much larger than the vorticity concentrations. Comparisons of the corresponding timeline

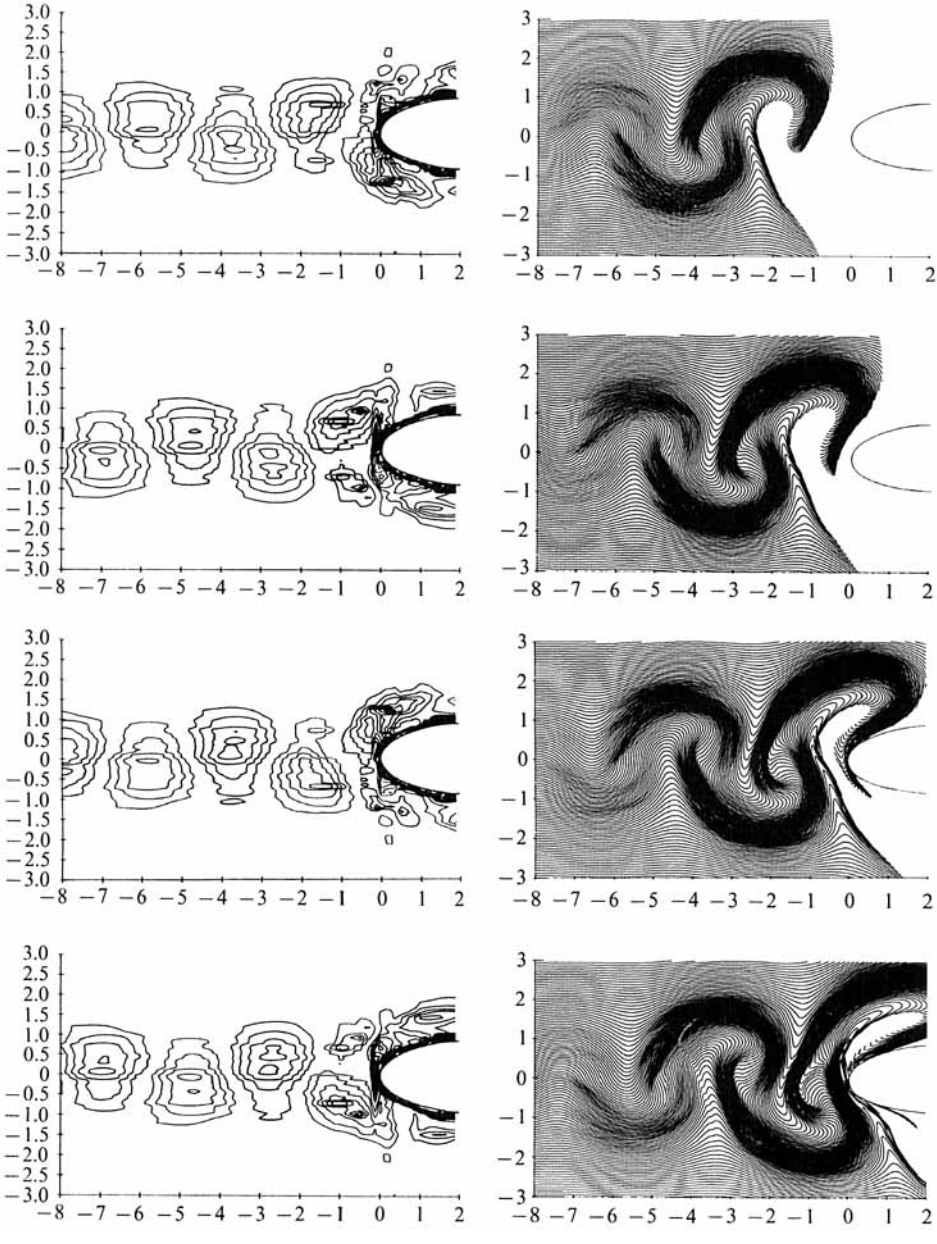

FIGURE 14. Vorticity contours (left-hand column) and streakline patterns (right-hand column) at successive times $t/T = 1.5$, 1.75, 2.00 and 2.25.

patterns with the streakline patterns is given in figure 15. These patterns are very similar.

Since the unsteady flow field near the body is not that of a neutral disturbance, it is expected that the location of injection of the marker will be important. Figure 16(*a*) shows the vorticity contours at instant $t = 0$ used as a basis for simulating streakline and timeline visualization. In figure 16(*b*), the timeline patterns are shown for different locations of the marker probe. It should be emphasized that the vorticity field is the same for both cases. Corresponding streakline patterns are

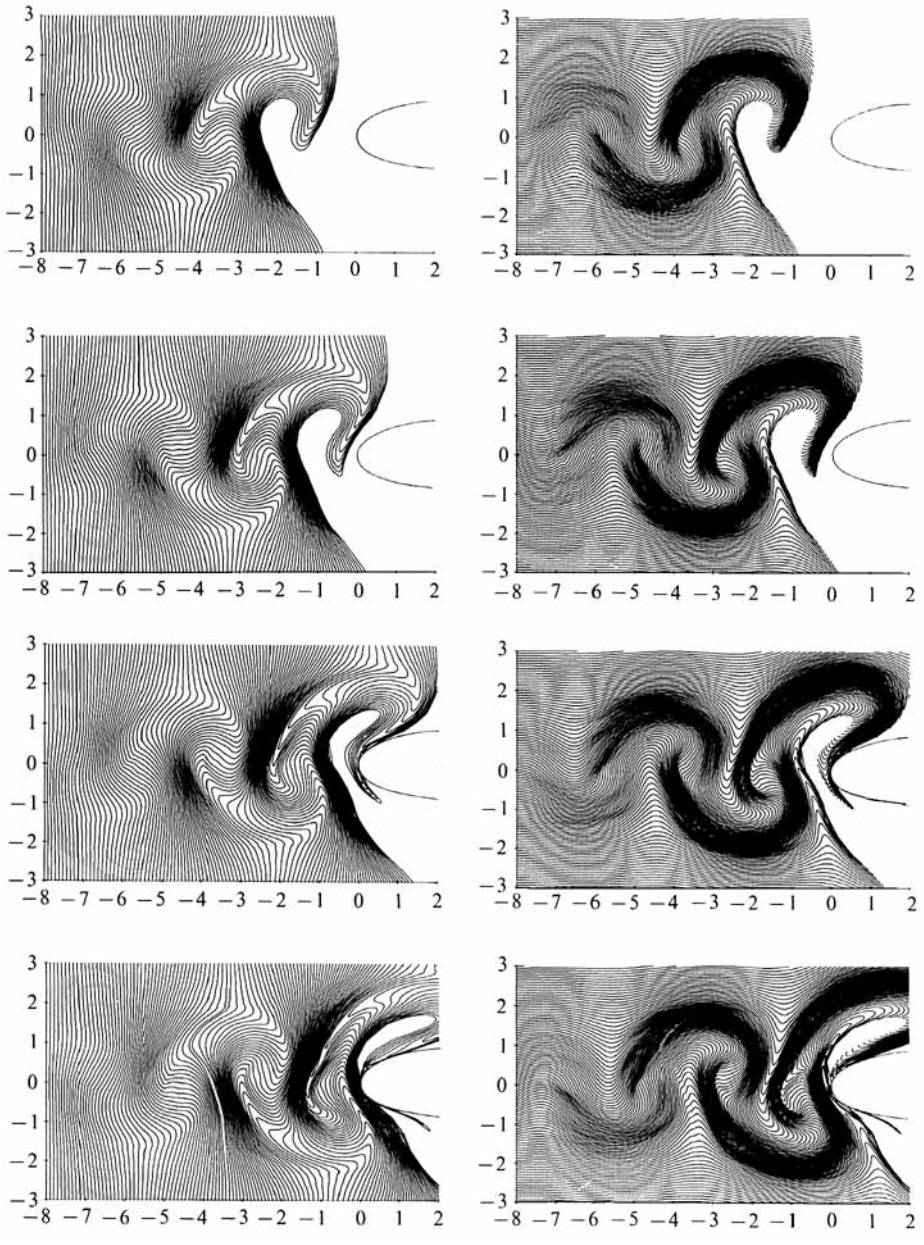

FIGURE 15. Timeline and streakline patterns at successive times $t/T = 1.5$, 1.75, 2.0 and 2.25.

shown in figure 16(*c*). For 'wire' or 'marker probe' locations closer to the body, it becomes more difficult to relate the visualized flow field to the prescribed vorticity field of figure 16(*a*) because of the amplifying appearance of the streaklines and timelines. It is therefore concluded that the 'marker probe' should be located sufficiently far upstream of the body to allow the markers to 'roll-up'. Otherwise, the estimated location of the vorticity concentrations can lead to very erroneous interpretations.

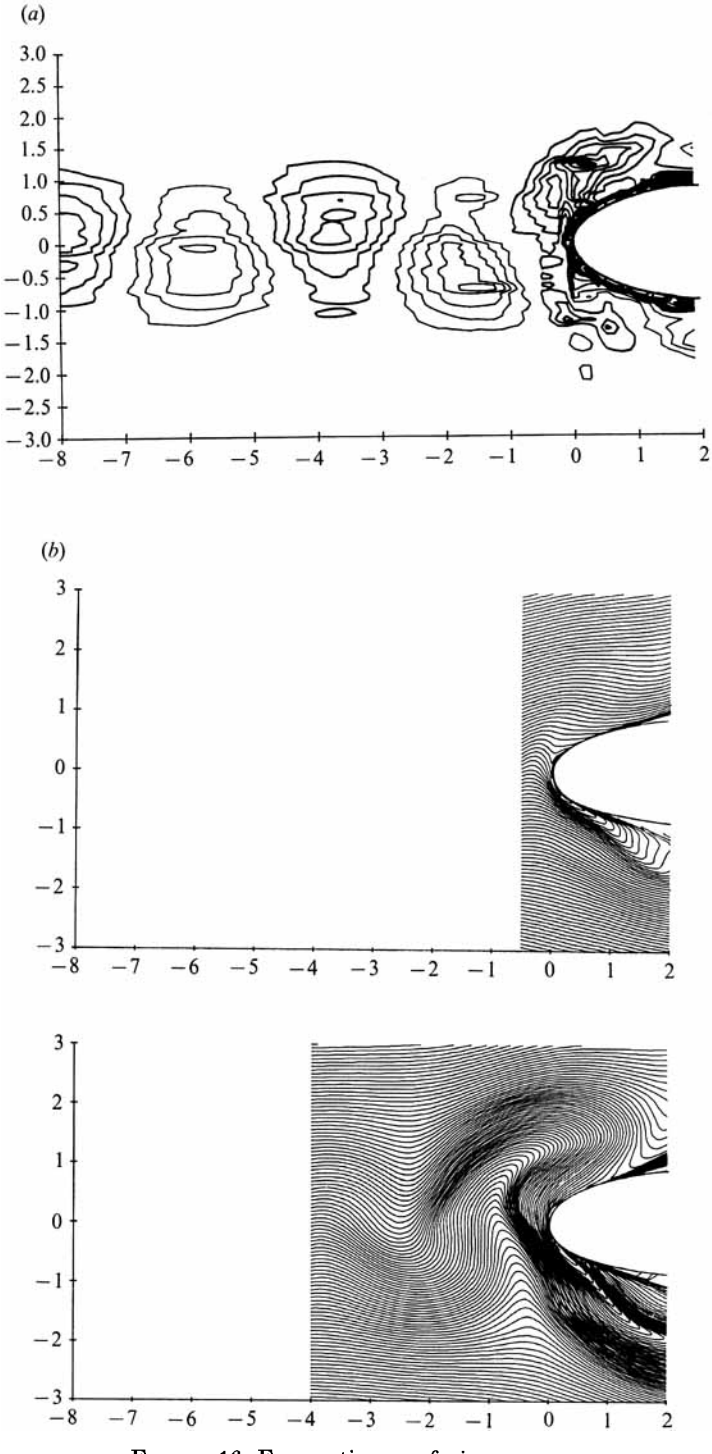

FIGURE 16. For caption see facing page.

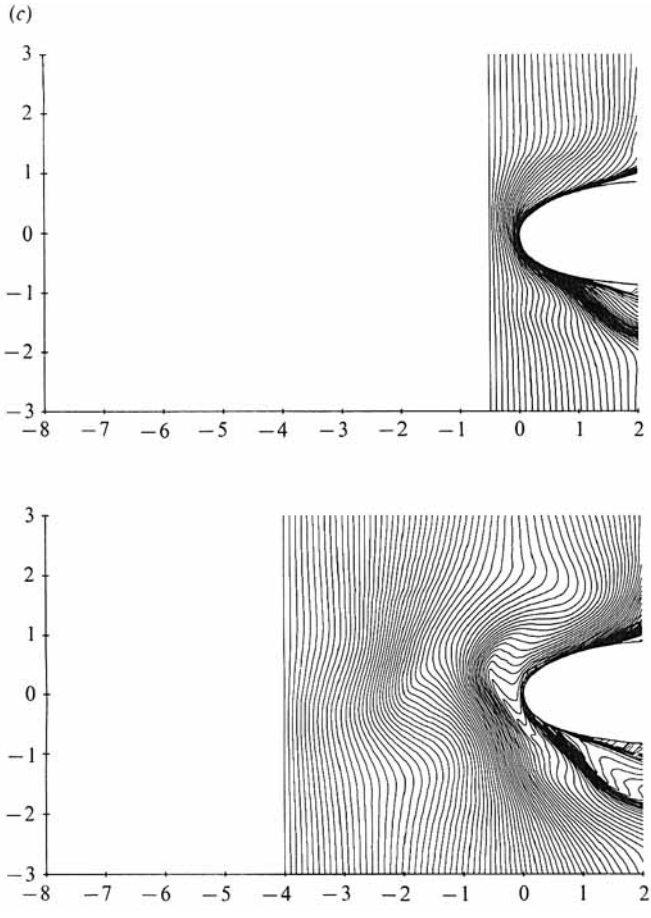

FIGURE 16. (*a*) Vorticity contours at the instant of simulated visualization. (*b*) Timeline patterns for different streamwise locations of marker probe. In both cases, flow field is the same, as defined by vorticity contours of (*a*). (*c*) Streakline patterns for different streamwise locations of marker probe. In both cases, flow field is the same, as defined by vorticity contours of (*a*).

7. Conclusions

It has been shown that there are a variety of possible vortex street–edge interactions depending on the lengthscales of the incident vorticity field and the edge. Important parameters are the transverse offset ϵ, the half-thickness of the edge H and the wavelength λ_∞ in the undisturbed vortex street which was varied by using different upstream plates. It is possible to classify these flow–edge interactions using the dimensionless scale λ_∞/H. Two representative scales were studied; they were designated as 'small-' and 'large-' scale vortex streets. Three basic interaction mechanisms were observed: (*a*) the vortex street preserved its identity; (*b*) the vortex street was split into two separate single rows of vortices; (*c*) each vortex in one row of the vortex street was split and its coherence was lost. The first two of these mechanisms were observed for both the small-scale and large-scale vortex streets, whereas the last one is possible only for the large-scale street.

These interactions gave rise to different types of wave-like unsteady pressure fields on the body, which were reconstructed by using a phase-averaging technique and related to the visualized flow patterns. The order of magnitude of the pressure

fluctuation amplitude varies strongly with the dimensionless lengthscale λ_∞/H of the incident vorticity field as well as with the dimensionless transverse offset $\epsilon/2H$. In the case where the vortex street preserved its identity, general features of the phase-averaged pressure field are in accord with inviscid simulations employing discrete vortices. For the other types of interaction, the distributions of pressure amplitude show substantial departure from what is expected based on simple simulations; there occurs a pronounced peak near the tip region of the edge. Regarding the pressure distribution over the edge, the present case is fundamentally different than those of Kaykayoglu & Rockwell (1985, 1986). In the case of a sharp edge, the pressure has maximum amplitude at the tip or downstream of the tip depending on the location of the boundary-layer separation and secondary vortex formation. However, in the present experiments there is no boundary-layer separation and the pressure is only due to the passage of the incident vortices.

Measurements of amplitudes and phase angles of the unsteady velocity field provided the phase-averaged flow field for a basic, generic interaction of the vortex street with the edge. The streamline patterns give different impressions depending on the reference frame in which they are viewed; closed streamlines near the body may not be attainable for any reference frame owing to the large transverse velocity component near the leading edge. The calculated vorticity field (from velocity measurements) revealed that the distortion of vortical structures takes place in a distance of about half a wavelength from the edge. During the distortion, the vortices are deformed into ellipses with their major axes parallel to the mean flow around the edge. While the vortices are swept along the surface, near the tip of the edge they are subject to rapid elongation in the cross-stream direction, resulting in large vorticity fluctuations around the tip of the edge. No boundary-layer separation was observed because of the low value of the vortex Reynolds number $Re = \Gamma/\nu$. The pressure field calculated from the measured velocity field by using the Poisson equation showed the essential features of the surface pressure distribution.

Because of its use in this study and its fundamental importance, flow visualization of this generic interaction was simulated using the measured velocity field. This simulation confirmed that the location of injection of the marker must be considered in interpreting the flow visualization for vortex–edge interactions. When the wire is located very close to the leading-edge, the streaklines have an amplifying appearance before they reach an equilibrium. On the other hand, if the wire is located well upstream, the visualized flow in downstream regions may have little to do with the real flow.

The stay of I.G. at Lehigh University was initially made possible through a Fulbright Scholarship administered by the Institute of International Education (IIE). This research program was funded by grants from the National Science Foundation and the Office of Naval Research. Supplemental support of the Volkswagen Foundation was instrumental in the initial phases of the flow visualization.

REFERENCES

BETCHOV, R. & CRIMINALE, W. O. 1967 *Stability of Parallel Flows*. Academic.

CERRA, A. W. & SMITH, C. R. 1983 Experimental observation of vortex ring interactions with fluid adjacent to a surface. *Rep.* FM-4, *Dept Mech. Engn*, Lehigh University, Bethlehem, PA.

CIMBALA, J. M., NAGIB, H. M. & ROSHKO, A. 1988 Large structure in the far wakes of two-dimensional bluff bodies. *J. Fluid Mech.* **190**, 265–298.

CONLISK, A. T. & VELEY, D. 1985 The generation of noise in impinging vortex motion past a step. *Phys. Fluids* **28**, 3004–3012.

DAVENPORT, A. B. 1977 The prediction of the response of structures to gusty wind. *Intl Res. Seminar on Safety of Structures under Dynamic Loading, Norwegian Institute of Technology.*

DAVIES, M. E. 1976 A comparison of the wake structure of a stationary and oscillating bluff body, using a conditional averaging technique. *J. Fluid Mech.* **75**, 209–231.

DIDDEN, N. & HO, C. M. 1984 Unsteady separation in a boundary layer produced by an impinging jet. *J. Fluid Mech.* **160**, 235–256.

DOLIGALSKI, T. L. & WALKER, J. D. A. 1984 The boundary layer induced by a convected two-dimensional vortex. *J. Fluid Mech.* **139**, 1–28.

ERSOY, S. & WALKER, J. D. A. 1985 Viscous flow induced by counter-rotating vortices. *Phys. Fluids* **28**, 2687–2698.

GURSUL, I. 1988 Interaction of Kármán vortex street with a leading edge. PhD thesis, Lehigh University.

GURSUL, I., LUSSEYRAN, D. & ROCKWELL, D. 1989 On interpretation of flow visualization of unsteady shear flows. *Expts Fluids* (in press).

HAMA, F. R. 1962 Streaklines in a perturbed shear flow. *Phys. Fluids* **5**, 644–650.

HARVEY, J. K. & PERRY, F. J. 1971 Flow field produced by trailing vortices in the vicinity of the ground. *AIAA J.* **9**, 1659–1660.

HUSSAIN, A. K. M. F. 1986 Coherent structures and turbulence. *J. Fluid Mech.* **173**, 303–356.

IMAICHI, K. & OHMI, K. 1983 Numerical processing of flow-visualization pictures-measurement of two-dimensional vortex flow. *J. Fluid Mech.* **129**, 283–311.

KAYKAYOGLU, R. 1987 Modelling of unsteady pressure fields due to vortex-curved surface interactions by the method of discrete vortices. Submitted to the *Bull. Istanbul Tech. University.*

KAYKAYOGLU, R. & ROCKWELL, D. 1985 Vortices incident upon a leading-edge: instantaneous pressure fields. *J. Fluid Mech.* **156**, 439–461.

KAYKAYOGLU, R. & ROCKWELL, D. 1986 Unstable jet–edge interaction. Part 1. Instantaneous pressure fields at a single frequency. *J. Fluid Mech.* **169**, 125–149.

LUGT, H. J. 1979 The dilemma of defining a vortex. In *Recent Developments in Theoretical and Experimental Mechanics.* Springer.

MATHIOULAKIS, D. S. & TELIONIS, D. P. 1987 Velocity and vorticity distributions in periodic separating laminar flow. *J. Fluid Mech.* **184**, 303–333.

MICHALKE, A. 1964 On the inviscid instability of the hyperbolic-tangent velocity profile. *J. Fluid Mech.* **19**, 543–556.

MORTON, B. R. 1984 The generation and decay of vorticity. *Geophys. Astrophys. Fluid Dyn.* **28**, 277–308.

NELSON, E. S. 1986 Phase-averaged measurements of vortex interaction with a solid surface and the breakaway process. MS thesis, Illinois Institute of Technology.

PANARAS, A. G. 1985 Pressure pulses generated by the interaction of a discrete vortex with an edge. *J. Fluid Mech.* **154**, 445–461.

PANARAS, A. G. 1987 Numerical modelling of the vortex/airfoil interaction. *AIAA J.* **25**, 5–11.

PEACE, A. J. & RILEY, N. 1983 A viscous vortex pair in ground effect. *J. Fluid Mech.* **129**, 409–426.

PERRY, A. E., CHONG, M. S., LIM, T. T. 1982 The vortex-shedding process behind two-dimensional bluff bodies. *J. Fluid Mech.* **116**, 77–90.

ROCKWELL, D. 1983 Invited lecture oscillations of impinging shear layers. *AIAA J.* **21**, 645–664.

ROGLER, H. 1974 A mechanism of vorticity segregation. *Bull. Am. Phys. Soc.* 2, **19**, 1165.

SATO, H. & KURIKI, K. 1961 The mechanism of transition in the wake of a thin flat plate placed parallel to a uniform flow. *J. Fluid Mech.* **11**, 321–352.

SCHLICHTING, H. 1979 *Boundary Layer Theory.* McGraw-Hill.

SOHN, D. Y. 1985 Vortex interaction with a leading edge of finite-thickness. MS thesis. Lehigh University.

ZABUSKY, N. J. & DEEM, G. S. 1971 Dynamical evolution of two-dimensional unstable shear flows. *J. Fluid Mech.* **47**, 353–379.

ZIADA, S. & ROCKWELL, D. 1982 Vortex–leading edge interaction. *J. Fluid Mech.* **118**, 79–107.